ANUL XLVIII **2003**

S T U D I A

UNIVERSITATIS BABEŞ–BOLYAI

PHYSICA

2

Editorial Office: Republicii no. 24, Cluj-Napoca, Romania. Phone: 0264-405352

SUMAR ■ SOMMAIRE ■ CONTENTS ■ INHALT

STUDIA UNIVERSITATIS BABEŞ-BOLYAI, PHYSICA, XLVIII, 2, 2003

DOSE DISTRIBUTION IN THE IRRADIATION OF MEDULLOBLASTOMA WITH TWO ADJACENT FIELDS

C. CUDALBU[1], A. STAN[2], O. COZAR[1], D. RISTOIU[1]

[1] "Babes-Bolyai" University, Cluj-Napoca;
[2] Oncological Institute "Prof. Dr. I Chiricuta" Cluj-Napoca

ABSTRACT. In this paper we analyse the absorbed dose distribution for the irradiation with two adjacent fields in the case of medulloblastoma treatment having in view the secondary effects of the irradiation at the sensitive organs level such as the cord and lung. The proposed objectives are: to achieve dose uniformity in the field junction region; to avoid the underdosage or overdosage in the junction area; the hot spot created due to the overlap of the beams at the depth has to be clinically acceptable; the dosage received by a sensitive structure such as the spinal cord must not exceed its tolerance dose.The analysis by geometric and dosimetric points of view shows that at the cord and lung level exists the risk of an important overdosage. This inconvenient can be solved by using three adjacent fields for irradiation.

1. Introduction

Because the special irradiation technique with adjacent fields is the most used in the case of medulloblastoma treatment, we consider very important to specify some general information about medulloblastoma.

This malignant disease has a large incidence to children with the age between 5-7 years. This tumor usually originates in the cerebellum and is referred to as primitive undifferentiated tumor. It may spread contiguously to the cerebellar peduncle, floor of the fourth ventricle, into the cervical spine. In addition, it may spread via the cerebrospinal fluid intracranially and/or to the spinal cord. For this purpose it is necessary to perform a treatment technique with cranial tangential fields combined with adjacent fields for the entire spinal cord to achieve a perfect coverage of the zones with malignant cells. [1]

The machine used in this study is the Co^{60} Unit Theratron 1000E, from Oncological Institute "Prof. Dr. I. Chiricuta", Cluj-Napoca, Romania.

We also use the "Treatment planning" system: Theraplan Plus, which processes the dosimetrical dates of irradiation machines and finally offers the doses distributions for a real case.

2. Experimental

2.1. The separation of adjacent fields

The entire subarachnoid space is considered of high risk in medulloblastoma, and has to be totally irradiated. The combination between an aggressive chemotherapy treatment and an incomplete craniospinal irradiation can be associated with a high rate of recurrence.

We identify two phases of the treatment technique: the craniospinal irradiation and the irradiation of the entire spinal cord of the child (Fig. 1). [2]

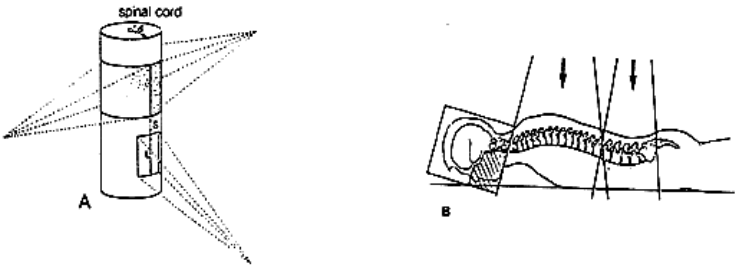

Fig. 1. (A)- 1 craniospinal field + 1 posteriospinal field; (B)- 1 craniospinal field + 2 posteriospinal fields.

In this paper we pay much more attention to the junction area from the posterior spinal adjacent fields, because it presents much more interest from the dosimetric points of view (because of the implications in distribution of doses generated by the beams divergence). So, the irradiation of the entire spinal cord is done with one or two fields for children with a higher age.

We have also, to pay attention to the dosage received by the sensitive structures (cord and lung), which enter in the posterior irradiation fields. [3, 4]

Across the junction region there is a possibility of introducing very large dosage errors. For this, the junction area is at risk for sever complications if it is overdosed, or for tumor recurrence if it is underdosed. [5]

When the tumor is superficial at the junction point the fields are usually abutted at the surface. However in this case we must be carefully at the hot spot created due to the overlap of the beams at depth. On the other hand, the fields can be separated on the surface for the treatment of deep-seated lesions (in the thorax, abdomen, and pelvis). In this case we place the beam so, that the cold spots created by the field separation will be located superficially, where it is no tumor [2, 6].

2.2. The geometric description of the fields separation

The dose at the point of junction between the beams will add up to be 100% if the geometric boundary of the field is defined by the 50% decrement line. The dose above the junction is lower and below the junction is higher than the junction dose if the two fields are incident from one side only and made the junction at a given depth. Fig. 2 illustrates the geometry of two adjacent fields, separated by a distance S_1+S_2 on the surface and junctioning of the depth d.

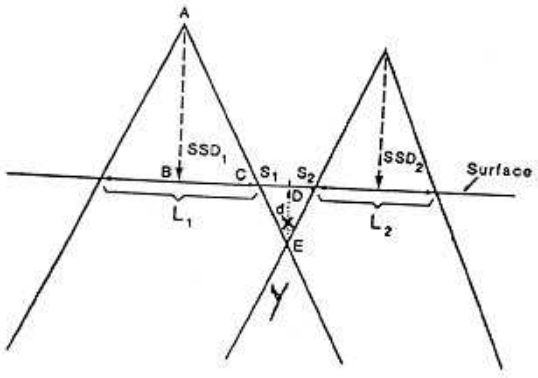

Fig. 2. Geometry of two adjacent beams, separated by a distance S_1+S_2 (L_1, L_2-field lengths; SSD_1, SSD_2-source-surface distance).

To determinate $S=S_1+S_2$ for obtaining a homogeneous dose distribution, we use the fact that the two triangles ABC and CDE are similar:

$$\Delta ABC \sim \Delta CDE$$

$$\frac{CD}{DE} = \frac{BC}{AB}$$

$$\frac{S_1}{d} = \frac{L_1}{2} \cdot \frac{1}{SSD_1}$$

$$S_1 = \frac{1}{2} \cdot L_1 \cdot \frac{d}{SSD_1}$$

$$S_2 = \frac{1}{2} \cdot L_2 \cdot \frac{d}{SSD_2}$$

$$S=S_1+S_2=\frac{1}{2} \cdot L_1 \cdot \frac{d}{SSD_1} + \frac{1}{2} \cdot L_2 \cdot \frac{d}{SSD_2}$$

From the first analysis we observe (Fig. 2.) that the X zone is underdosed and the Y zone is overdosed.

The relevant factors that make this problem one of the most complex in radiotherapy are: patient positioning, beam alignment, field penumbra and radiation scatter. [7]

For a composite uniform isodose distribution at the desired depth and an acceptable cold and hot spots, the separation of fields can be determinated by optimizing the placement of fields on the contour. The accuracy of the individual field isodose curves especially in the penumbra region has a big influence on the accuracy of this procedure. [8]

3. Results and discussions

For this particular case we have analysed the spinal irradiation because the phenomenum treated in this study was better evidenced than in any other region.

The child has a largest spinal cord and we have done the treatment plan by using two and three adjacent fields. After the simulation of the patient and put in evidence of organs of interest (vertebrae, cord, lung) we have started to simulate the treatment plan with the Theraplan Plus treatment planning system, following the purposes that we plane to achieve in the junction area.

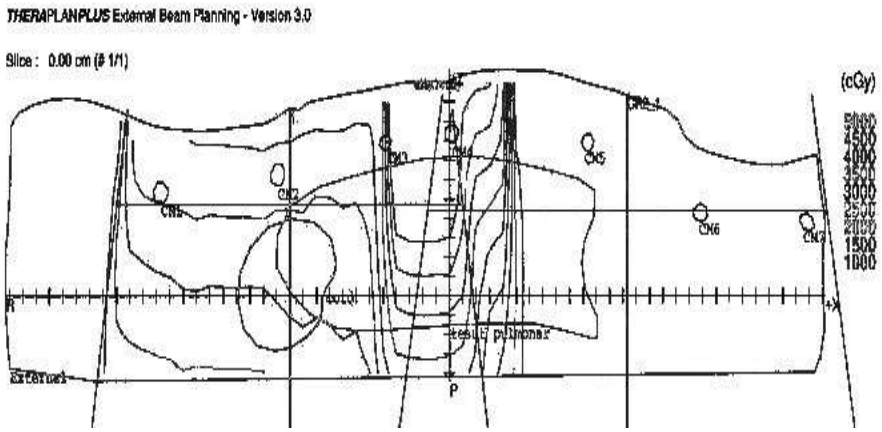

Fig. 3. Dose distributions for an irradiation with two adjacent fields, without corrections.

Fig. 3 illustrates the irradiation of the entire spinal cord using two adjacent fields. We situate the vertebrae 4, in the junction region of the two fields. As can be seen from the isodose map (Fig. 3.) the vertebrae 4 is in a hot spot, where the contributions of the beams are summed because the fields are abutted.

Because the total dose administrated in therapeutical purpose is 5000 cGy and we want to achieve a proportion 95-105% of this, the value of 6497 cGy received by the vertebrae 4 needs an optimization of this treatment plan.

Table 1.

Dose statistics for Fig. 3

STRUCTURE	MIN (CGY)	MAX (CGY)	AVERAGE (CGY)
External	53.89	8234.74	1644.21
CM1	2527.37	2527.37	2527.37
CM2	2759.16	2759.16	2759.16
CM3	3449.66	3449.66	3449.66
CM4	6497.12	6497.12	6497.12
CM5	200.62	200.62	200.62
CM6	125.60	125.60	125.60
CM7	123.66	123.66	123.66
cord	1690.92	2456.91	2109.16
lung tissue	185.04	6471.79	2750.24

Plan Normalization 100% = 200.00
Prescription Dose (cGy) = 5000.00
Prescription – Isoline (%) = 100.00

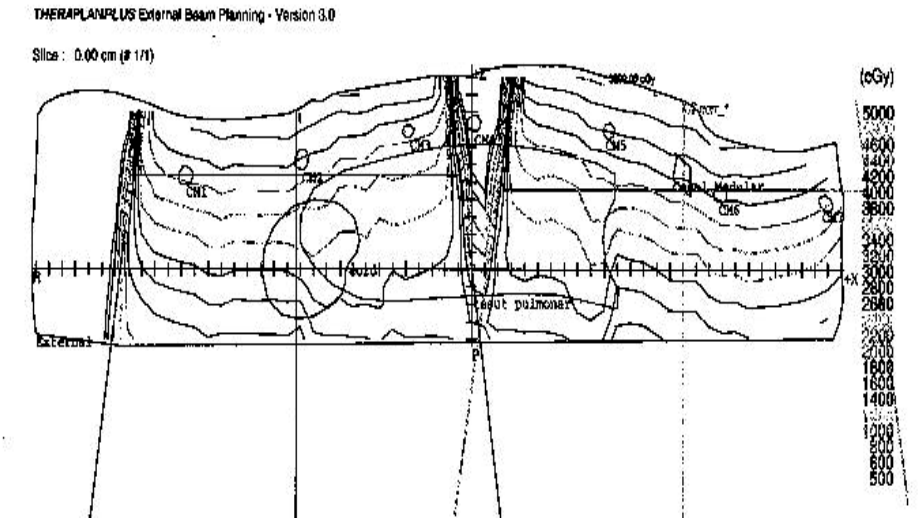

Fig. 4. Dose distributions for an irradiation with two adjacent fields with corrections.

Fig. 4 shows a much fiabel irradiation plan because in this case we take into account the divergence of the beams. The vertebra 4 was put intentionally out from the both fields, so in the final phase it is situated in cold spot, where the contribution of the beams is minimal. In this case the value of 279 cGy is not enough and for this we do this treatment until we reach 25% from the total dose. After this the entire therapeutically arrangement is translated situating the next vertebrae in the cold spot. We repeat this procedure until the total dose in the spinal cord is homogeneous.

Table 2.

Dose statistics for Fig. 4

STRUCTURE	MIN (CGY)	MAX (CGY)	AVERAGE (CGY)
External	66.79	3299.00	1827.75
CM1	2394.26	2394.26	2394.26
CM2	2549.19	2549.19	2549.19
CM3	2519.22	2519.22	2519.22
CM4	279.28	279.28	279.28
CM5	2809.52	2809.52	2809.52
CM6	2617.28	2617.28	2617.28
CM7	2441.78	2441.78	2441.78
cord	1571.99	2246.01	1928.50
lung tissue	322.76	2462.25	1840.21
medullar channel	2571.63	2720.55	2646.09

Plan Normalization 100% = 200.00
Prescription Dose (cGy) = 5000.00
Prescription – Isoline (%) = 100.00

It is necessary to do some observation now about the absorbed dose in the critical organs (cord and lung). Because in these vital organs the absorbed dose has to be not more than 5000 cGy, the irradiation technique has to be reported to this important factor. So, where the dose in the critical organs is very high we do an optimization of the irradiation plan until we reach normal values in cord and lung, even with the risk of decreasing the total dose in the spinal cord. But this is a solution in extremis. Another solution is what we call personalized protection for the critical organs, which not affects the dose in the points of interest.

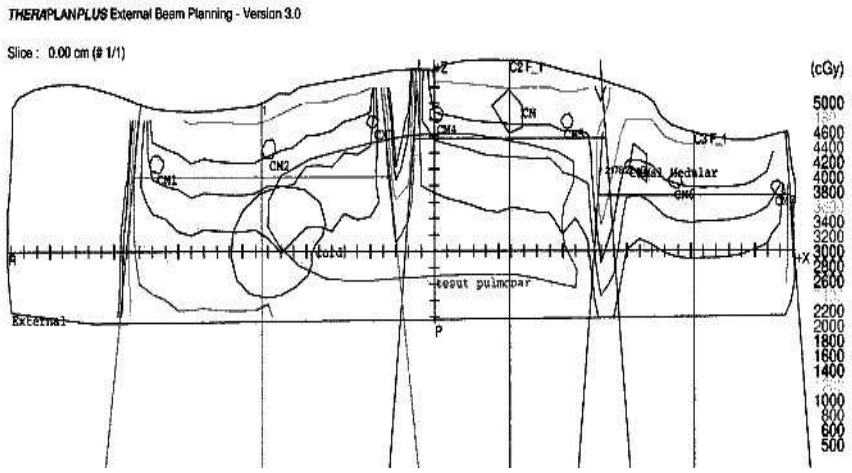

Fig. 5. Dose distributions for an irradiation with three adjacent fields.

Table 3.

Dose statistics for Fig. 5

STRUCTURE	MIN (CGY)	MAX (CGY)	AVERAGE (CGY)
External	20.57	2176.22	1264.31
CM1	1644.00	1644.00	1644.00
CM2	1819.62	1819.62	1819.62
CM3	1761.28	1761.28	1761.28
CM4	1767.99	1767.99	1767.99
CM5	1872.36	1872.36	1872.36
CM6	1796.61	1796.61	1796.61
lung tissue	440.11	1667.70	1300.19
medullar channel	1753.43	1847.90	1800.66
CM	1834.16	1920.32	1888.08

Plan Normalization 100% = 300.00
Prescription Dose (cGy) = 5000.00
Prescription – Isoline (%) = 100.00

A significant decreasment of the dose in the critical organs with an optimal irradiation of the spinal cord is done by irradiating the spinal cord with three adjacent fields (Fig. 5.). So, we do a differentiated irradiation of the cervical, dorsal and lombar spinal cord. In this situation we had two junction areas.

4. Conclusions

The advantage of the irradiation technique with two adjacent fields used by us implies the local control of the absorbed dose in only one vertebra.

This special irradiation technique gives good results from both dosimetrical and reproducible point of view. By this way we obtained a curative treatment with a homogeneous dose in the entire spinal cord and a minimalization of the dose in the critical organs.

In the case of the irradiation with three adjacent fields the analysis of the absorbed dose has to be done at the level of two junctional vertebrae.

The irradiation with three fields is not recommended in the treatment of the meduloblastom for little children.

REFERENCES

1. C. Carrie, S. Hoffstetter, F. Gomez, Int. J. *Radiat*. Oncol. Biol. Phys., 45, 435 (1999)
2. Ghilezan, *Cobaltoterapia,* Ed. Medicala, Cluj-Napoca, 1983
3. K. Bratengeier, L. Pfrendner, M. Flentje, *Radiotherapy and Oncology*, 56, 209 (2000)
4. E.J. Holupka, J.T. Humm, N.J. Tarbell, G.K. Svensson, Int. J. *Radiat*. Oncol. Biol. Phys., 27, 345 (1993)
5. T.J. Endicott et al, *Radiotherapy and Oncology*, 60,267 (2001)
6. Khan F.M., *The Physics of Radiation Therapy,* 2nd ed., Williams&Wilkins, Baltimore, Tokyo, 1994
7. K.H. Pigott, S. Dische, B. Vojnovic, M.J. Saunders, *Radiotherapy and Oncology*, 49, 109 (1999)
8. M.H.M. Idsez, O. Holmerg, B.J. Mijnheer, H. Huizehga, *Radiotherapy and Oncology*, 46, 91 (1998)

STUDIA UNIVERSITATIS BABEŞ-BOLYAI, PHISICA, XLXVIII, 2, 2003

EVALUATION OF AN IMPLANTABLE PLANAR RF MICROCOIL PROTOTYPE FOR LOCALIZED NMR SPECTROSCOPY

M. ARMENEAN[1,2*], L. BERRY[3], O. COZAR[1], H. SAINT-JALMES[2]

[1]Babes-Bolyai University, Dept. of Physics,
1 Kogalniceanu, 3400 Cluj-Napoca, Romania
[2]Laboratoire de RMN, UMR CNRS 5012, Université
Claude Bernard Lyon 1 – ESCPE Lyon, 69622
Villeurbanne Cedex, France.
[3]LENAC JE 2266, Université Claude Bernard Lyon1–
bât. 203, 69622 Villeurbanne Cedex, France.

ABSTRACT. This paper reports the design, the fabrication and preliminary tests of planar microcoils used as Nuclear Magnetic Resonance radio-frequency detection coils. The magnetic coupling between a RF coil and a sample is maximized by physically designing the coil as small as possible as to just accommodate the sample. Maximum coupling corresponds directly to an optimal sensitivity for the signal reception. Designed for a biological application, these coils have to be as less invasive as possible and they must allow studying small quantities of metabolites surrounding the microcoil. NMR micro-spectroscopy experiments have been performed in water and butter samples using a 500×1000 μm² planar microcoil tuned and matched at 85.13 MHz (proton's frequency at 2 T).

1. Introduction

One of the most recent progresses in Nuclear Magnetic Resonance (NMR) is the in-vivo micro-spectroscopy and the analysis of small volume biological samples. These new fields require the reduction the size of the NMR radio-frequency detection coils [1, 2]. To succeed, two main approaches can be considered, i.e. solenoidal microcoils and planar microcoils. Solenoidal microcoils have already been studied [3] by the authors and have shown promising results in terms of detection efficiency and spectral resolution. But, in this case the more efficient zone for the detection is the center of the coil,

* E-mail : mircea@jade.univ-lyon1.fr
Tél. : + 33 4 72 44 80 84
Fax : + 33 4 72 44 81 99

which is not compatible with the implantable geometry for biological application. So, the planar microcoils are more adapted, because their detection zone is located just around the coil.

In this paper, we describe the design and fabrication of planar microcoils. Most of the coil fabrication steps are compatible with standard integrated circuit (IC) technologies and can be performed by a batch-process. This enables to consider a low cost mass production of NMR sensors and the integration of the electronic circuitry. In order to evaluate detection efficiency and spectral resolution, preliminary NMR micro-spectroscopy experiments have been performed using a planar microcoil tuned at 85.13 MHz under a static magnetic field of 2 T.

2. Planar microcoil fabrication

In order to increase the NMR Signal-to-Noise Ratio (SNR) and the quality factor Q of the RF coil it is necessary to work with a coil thickness as high as possible [4, 5, 6]. The recent progresses in electrochemistry precisely enable to deposit thick metallic layer of different nature. This cannot be achieved by standard sputtering or evaporation techniques which are typically limited to 1 μm in thickness. Here, copper as been chosen due to its good electrical conduction properties.

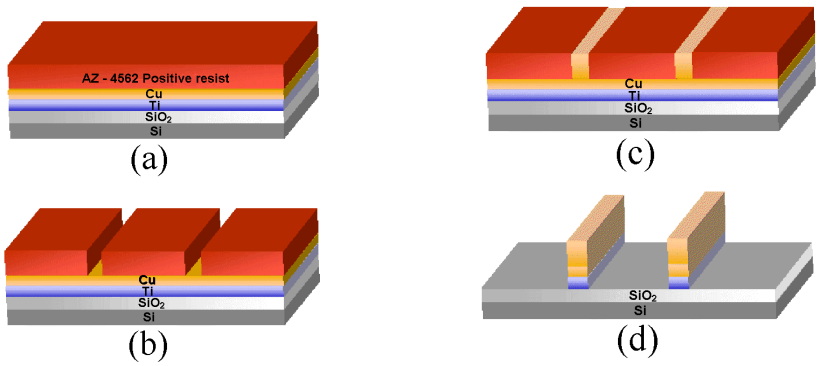

Fig. 1. *Fabrication steps of a planar microcoil.*

The starting material for the fabrication of planar microcoils is a n-type 4 inch silicon wafer (520 μm thick) with a one micron thermally grown SiO_2 oxide layer providing an electrical insulation. As

shown in Fig. 1a, a 20 nm Ti and 200 nm Cu seed layer is deposited by sputtering. The Ti layer is used to ensure a good mechanical adhesion of the copper layer. A 45 μm thick AZ - 4562 positive resist is subsequently deposited and developed using standard photolithography process (Fig. 1b), which is similar to the one used in reference [4].

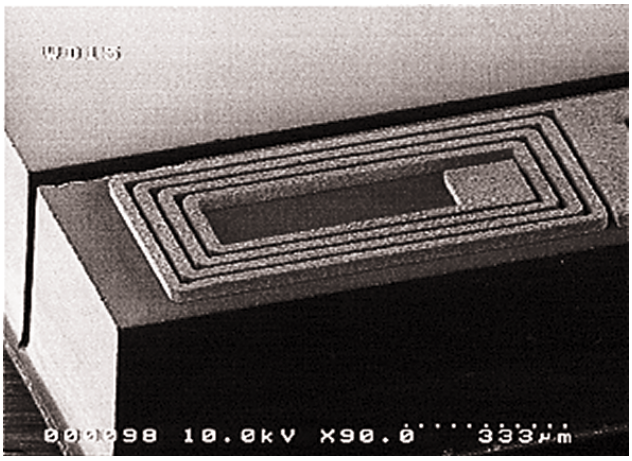

Fig. 2. SEM view of the planar microcoil.

The resist structure is then used as a mould during copper electroplating (Fig 1.c). The copper thickness can be adjusted with deposition time up to the resist thickness. The resist and the copper seed layers are subsequently removed in order to insulate the wires (Fig 1.d). Finally the silicon wafer is cut with a die saw to form one cm long needles (Fig. 2) with the 1000 μm×500 μm planar microcoil located at the tip of the needle. In this way, a minimally invasive introduction of the coil in a living biological tissue is enabled.

3. Simulated charateristics of the microcoil

For calculating not only the quality factor (Q) but also the signal-to-noise ratio (SNR), we simulated the electromagnetic parameters (the electrical resistance R_{noise}, the inductance L and the RF field B_1) of a planar rectangular RF microcoil using ANSOFT Maxwell 2D/3D software (Ansoft Corp., Pittsburgh, USA) and Magnetic@ (MagneticaSoft, Nice, France). The Maxwell 2D/3D software is based on advanced finite element technology and uses electromagnetic AC and DC field simulation to predict product

performance with physical and geometric input. Magnetic@, works under Mathematica software (Wolfram Research, Inc., USA) and provides high accurate computations of static magnetic field [7]. This software offers the choice of two modes of calculation: a method derived from the vector potential which is applicable to all space including the winding and the magnetic materials and a method using spherical harmonics which is restricted to the space without magnetic field generator.

The simulations have been performed using magnetostatic and AC magnetic approximation in order to calculate the B_1 field and the inductance L, and sinusoidal excitation (85.13 MHz) of the RF coil in order to calculate the resistance R_{noise} of the coil. The axial component of the magnetic field produced by a microcoil with length = 1000 µm, width = 500 µm, number of turns = 4, distance between two adjacent turns = 20µm, wire thickness = 38 µm and wire width = 22 µm, for a current I = 1 A is given in Fig. 3.

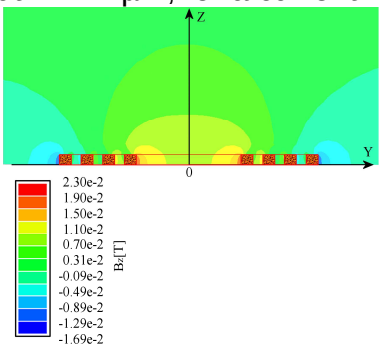

Fig. 3. The axial component of the magnetic field produced by a microcoil with a length of 1000 µm, a width of 500 µm, four turns, a distance between two adjacent turns of 20 µm, a wire thickness of 38 µm and a wire width of 22 µm, for a current I = 1 A

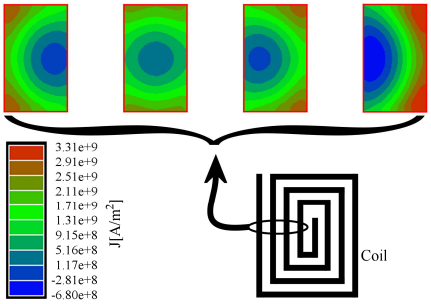

Fig. 4. The distribution of the current density J, for a current I = 1 A at 85.13 MHz in the cross section of microcoil.

The SNR of a NMR experiment is defined as the peak signal divided by the root mean square (rms) noise [8]:

$$SNR = \frac{\text{peak signal}}{\text{RMS noise}} = \frac{\frac{B_1}{i}\omega_0 M_0 V_S}{\sqrt{4kTR_{noise}\Delta f}} \quad (1)$$

with:

$$M_0 = \frac{N\gamma^2\hbar I(I+1)B_0}{3kT} \quad (2)$$

where B_1/i is the magnetic field per current unit (*coil sensitivity*), ω_0 the nuclear precession pulsation, M_0 the nuclear magnetization, V_S the sample volume, k the Boltzmann's constant, T the sample temperature, N the spin density, γ the gyromagnetic ratio, I the spin quantum number, $\hbar$ the Planck's constant divided by 2π, B_0 the static magnetic field and Δf is the spectral bandwidth. R_{noise} is the total resistance of the coil, which includes the magnetic losses. According to (1), the performances of the RF receiver coils are driven by the ratio $B_1 / i\sqrt{R_{noise}}$.

At reduced dimensions of the sample, the noise originating within the sample is negligible when compared to the noise of the coil [9, 10]. In this condition, the noise due to the sample resistance is usually small compared to the noise due to the microcoil resistance ($R_{noise} \approx R_{coil}$). The electrical resistance of the microcoil R_{coil} is increased by the skin effect and the proximity effect in the coil wires. The current is concentrated towards the outer edge of the conductor (skin effect) with the current density decreasing exponentially from the wire surface to the center. The magnetic field lines from a given turn of coil induce eddy currents in adjacent turns (proximity effect), further distorting the current distribution and increasing the resistance of coil [10, 11].

The computation of the electrical resistance R_{coil} for planar microcoils is complicated by the fact that in the case of a wire with rectangular sections, standard calculations rules are no more relevant and the help of electromagnetic simulation software is mandatory in order to obtain accurate results. For the wires with rectangular section, the current is not uniformly distributed at the

surface like in the case of wires with circular section. This effect is more accentuated when the ratio between the sides of rectangular section increases. The distribution of the current density J for a current I = 1 A at 85.13 MHz in the cross section of microcoil (with the same geometric parameters) is shown in Fig. 4.

The quality factor Q and the signal-to-noise ratio SNR were computed for proton in water at B_0 = 2 T (f = 85.13 MHz), T = 20 °C and Δf = 10 kHz.

The calculated inductance and electrical resistance of the active region of microcoil (see Fig. 5) are L ≈ 15.6 nH and R ≈ 0.424 Ω. Taking in to account the electromagnetic characteristics of the connection circuit (3.8 nH, 0.296 Ω) and the bounding wire (0.037 Ω), the total inductance and the total electrical resistance of the coil are L_{coil} ≈ 19.4 nH, respectively R_{coil} ≈ 0.757 Ω. The values of the quality factor Q and the signal-to-noise ratio SNR were calculated to be approximately 14, respectively 110.

4. Experimental results

The geometric characteristics of the microcoil which has been evaluated are the following: length = 1000 µm, width = 500 µm, number of turns = 4, distance between two turns = 20µm, wire thickness = 38 µm and wire width = 22 µm.

In order to optimize the NMR signal transmission through a coaxial cable, a conventional tuning-matching circuit has been used (Fig. 5). The coil was tuned at 85.13 MHz (proton's resonance frequency at 2T) and matched at 50 Ω for this frequency. According to fig 5, the planar microcoil was immersed in the sample and only used as NMR receiver, while a large RF coil surrounding the sample was used for the excitation. The two radiofrequency field directions (excitation and reception) are orthogonal (see fig. 5) ensuring a good geometrical decoupling.

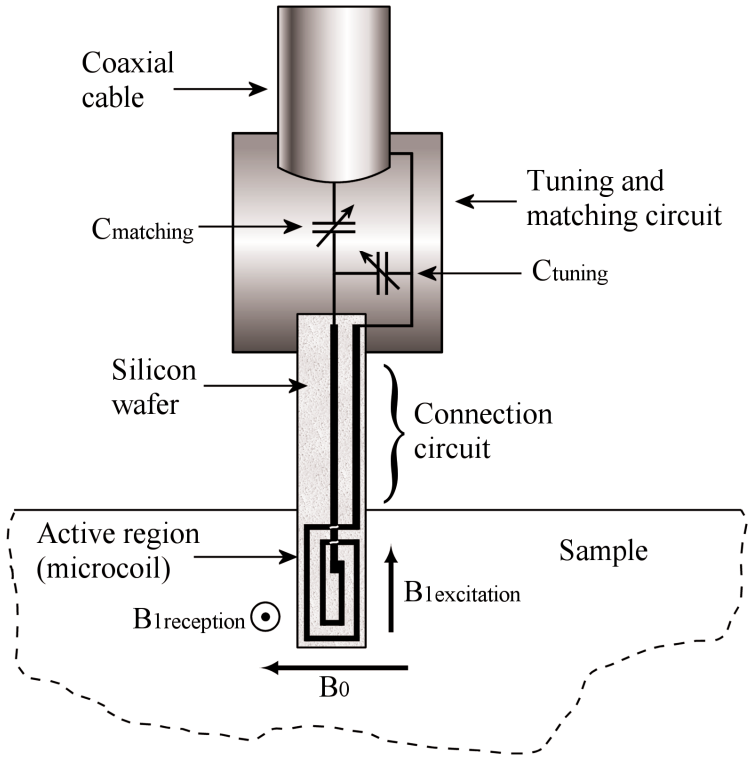

Fig. 5. Schematic representation of implantable planar microcoil and experimental conditions (B_0 is the 2 T static magnetic field).

Electromagnetic characterization of the microcoil was performed using a HP 4195A network analyzer. The measured quality factor Q at 85.13 MHz is approximately 10. This value is less than expected from simulations because it is very difficult to calculate the losses due to the silicon wafer, the coaxial cable, the imperfections of solders and the tune/match circuit. The investigated coil don't have a self – resonance in 10 MHz – 500 MHz spectrum of frequencies which allow to use this antenna in high frequencies spectroscopy.

In a first experiment, the planar microcoil was immersed in a small deionized water sample (0.33 cm^3) in order to obtain the Proton spectrum of water (Fig. 6). With 4 averages (corresponding to a scan time of 6 s), the SNR and the FWHM are 95 and 33 Hz respectively.

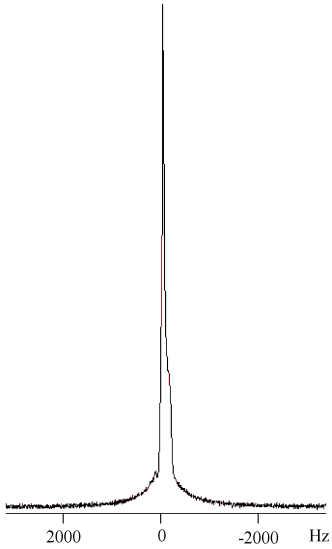

Fig. 6. ^{1}H NMR spectra of a deionized water sample at 2 T.

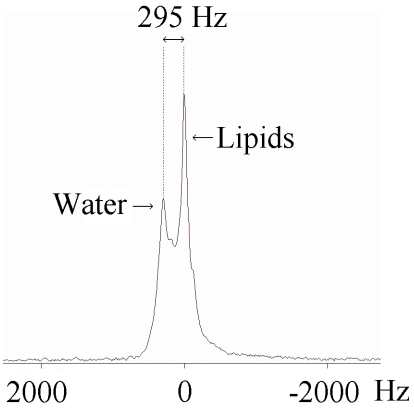

Fig. 7. ^{1}H NMR spectra of a lipid compound sample (butter) at 2 T.

The microcoil was then immersed in a small butter sample (0.33 cm^3) in order to have a better evaluation of the spectral resolution. Fig. 7 shows the Proton spectrum of a butter sample, which was acquired with 4 averages (corresponding to a scan time of 6 seconds). The spectra enable to distinguish water group from (CH_2-CH_3) fat group. The difference in frequency between water and lipids is 295 Hz, which corresponds to 3.5 ppm. This result is in agreement with a similar experiment with a solenoidal NMR microcoil [3].

Another interesting point of these first experiments is the evaluation of the measured volume of sample by the planar microcoil. This volume can be deduced from three orthogonal 2D NMR images projections of an homogeneous sample by the microcoil, some butter in our case. MR images were obtained using a gradient-echo sequence. Imaging parameters were: TR/TE 1000/21 ms; FOV = 50 mm, 3 mm slice thickness; 128 x 64 matrix; 20 kHz sampling rate and number of averages AVE = 4. Fig. 8 shows that the measured zone of the sample is limited in the space just around the microcoil,and is experimentally approximated to 5 µl.

5. Conclusion and perspectives

These first results have validated the miniaturization of the NMR spectroscopy experiment with planar microcoils. This represents a significant advance in the field of in-vivo NMR spectroscopy. Indeed, this microcoil allows making NMR spectroscopy of small volume samples (a few µl) with an acceptable spectral resolution (a few ppm). The difference in susceptibilities of the different materials located near the microscopic sample creates B_0 magnetic field distortions which are responsible for this spectral broadening [7].

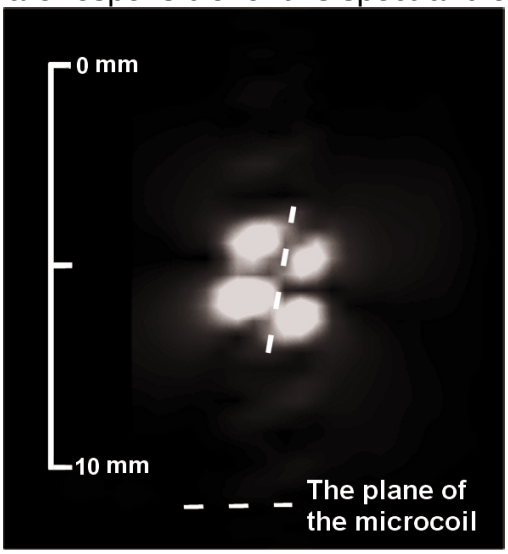

Fig. 8. ^{1}H coplanar NMR image of an homogeneous sample of butter by a planar microcoil.

The imperfection of images symmetry (fig. 8) is certainly due to some residual coupling between the emission RF coil and the receiving microcoil.

The good correlation between the calculated and measured values of the electromagnetic parameters for investigated microcoil valid the ANSOFT Maxwell 2D/3D software and Magnetic@ like a useful mean to predict the electromagnetic performances of microcoils.

For the next steps, microcoils designed with our simulation software will be tuned and matched at 34.46 MHz to detect ^{31}P in cerebral tissues during paradoxical sleep [12].

Acknowledgements

This work was performed within the framework of the Transnational Access to Major Research Infrastructures, part of the Human Potential Programme of the European Commission; with the financial support of the *programme thématique prioritaire de la région Rhône-Alpes*; and with the financial help of EZUS-LYON 1 (ANVAR).

We acknowledge the assistance and technical support of Linda Chaabane (Laboratoire RMN).

REFERENCES

1. J. D. Trumbull, I. K. Glasgow, D. J. Beebe and R. L. Magin, IEEE Trans. Biomedical Engineering, 47, 3, (2000).
2. J. Dechow, A. Forchel, T. Lanz, A. Haase, Microelectronic Engineering, 53, 517 (2000).
3. L. Berry, L. Renaud, P. Kleimann, P. Morin, M. Armenean, H. Saint-Jalmes, *Sensors and Actuators A: Physical*, 93, 214 (2001).
4. G. Boero, C. de Raad Iseli, P. A. Besse and R. S. Popovic, Sensors and Actuators, A67, 18 (1998).
5. C. R. Neagu, H. V. Jansen, A. Smith, J. G. E. Gardeniers and M. C. Elwenspoek, Sensors and Actuators, A62, 599 (1997).
6. A. P. L. Ling, Thesis, Hong-Kong University of Science & Technology, 1998.
7. L. Donadieu and H. Saint-Jalmes, *44th Annual Conference on Magnetism & Magnetic Materials*, San Jose, California USA, Nov. 15-18,1999.
8. D. I. Hoult and R. E. Richards, J. Magn. Reson., 24, 71 (1976).
9. D. L. Olson, T. L. Peck, A. G. Webb, R. L. Magin and J. V. Sweedler, Science, 270, 1967 (1995).
10. T. L. Peck, R. L. Magin and P. C. Lauterbur, J. Magn. Reson., Series B 108, 114 (1995).
11. A. G. Webb, Progress in NMR Spectroscopy, 31, 1-42 (1997).
12. R. Cespuglio, Rev. Neurol., 156 (3), 320 (2000).

STUDIA UNIVERSITATIS BABEŞ-BOLYAI, PHISICA, LXVIII, 2, 2003

SECONDARY STRUCTURE ANALYSIS OF C-TERMINAL DOMAIN IN HUMAN CENTRIN 2 BY NMR SPECTROSCOPY AND CIRCULAR DICHROISM

E. MATEI[A] , C. T. CRAESCU[B], P. DUCHAMBON[B], C. NICULESCU[B], Y. BLOUQUIT[B], S. SIMON[A]

[a]Babes-Bolyai University, Kogalniceanu 1, 3400 Cluj-Napoca, Romania
[b]INSERM U350 & Institut Curie - Recherche, Centre Universitaire,Bâtiments 110-112, 91405 Orsay, France

ABSTRACT. Analysis of two-dimensional NMR spectra recorded from isolated C-terminal domains of human centrine 2 (HCen2) offers information on the elements of its secondary structure. Five α helices (F89 - Q95, K103 –F113, F123 – E132, D139 – A149, E159 - K167) and an anti-parallel β-sheet (K120-S122, E156-S158) are identified. The two EF-hand motifs form a canonical structure, similar to the "open" forms of other Ca^{2+}-saturated regulatory domains. The structural stability and binding properties of HCen2 and its isolated domains are characterized using the circular dichroism spectroscopy. Comparative chemical stability studies reveal that the structure of the longer domain LC-HCen2 is considerably more stable than that of the shorter one SC-HCen2.

Introduction

EF-hand is a common structure to bind Ca^{2+} in calmodulin and other proteins consisting of a helix (E), a loop and another helix (F). Calmodulin is a Ca^{2+} binding protein involved in metabolic regulation. The human centrin 2 is a member of the EF-hand superfamily of Ca^{2+}-binding proteins, of about 20 kDa, including four EF-hand motifs. This protein was found to be localized into the major microtubule organizing center, in the centrosome, and is supposed to play a significant role during the cell duplication [1, 2]. Microtubules are conveyer belts inside the cells. They move vesicles, granules, organelles like mitochondria, and chromosomes via special attachment proteins. They also serve a cytoskeletal role. Structurally, they are linear polymers of tubulin that is a globular protein. These linear polymers are called protofilaments [3].

Like the majority of the Ca^{2+}-binding proteins of this molecular mass, centrin 2 is composed of two domains N-terminal and C-terminal, each containing two EF-hand motifs, connected by a long α-helix [4]. No three-dimensional structure of any centrin is presently available.

The aim of this study is to explore the correlation between structure and properties of human centrin 2, including structure determination, Ca^{2+} binding, physico-chemical properties and chemical stability using nuclear magnetic resonance (NMR) and circular dichroism (CD) spectroscopies.

Experimental

The samples for NMR spectroscopy (0.7–1.2 mM) were obtained by dissolving the lyophilized protein in deuterated Tris HCl buffer, pH 6.5 and 100 mM KCl (or NaCl). NMR spectra were recorded on a Varian Unity 500 NMR spectrometer, at 35°C. Standard homonuclear (COSY-DQF, TOCSY, NOESY) and heteronuclear (^{15}N-HSQC, ^{15}N-NOESY-HSQC) spectra were used for resonance assignment and collection of distances and angle restraints. Spectra analysis was done using Felix 230 software.

Circular dichroism spectra were recorded at 25°C on a Jasco 710 spectropolarimeter in the UV region (185-250 nm), using 1 mm quartz cell and sample concentrations of 20 mM diluted in Tris HCl buffer (10 mM), pH 7.6.

Results and discussion

Although the four EF-hand motifs could be easily identified in the primary structure of centrin, only one binding site per monomer (site IV) has a significant binding affinity for calcium ions in presence of Tris HCl buffer, 150 mM KCl [5]. Difficulties due to the dimerisation of the integral protein determined the present structural study on isolated domains. Similar studies on isolated domains of other calcium-binding proteins, such as calmodulin (CaM) [6] and troponin C (TnC) [7-9], have been successfully carried out. Two distinct sequences of 89 and 79 residues, representing the C-terminal half, were obtained by over-expression in *E. coli* and purification. The 89 residue domain (M84–Y172), named LC-HCen2, was obtained as a proteolysis product during the over-expression of the integral protein while the second C-terminal domain (T94–Y172), named SC-HCen2, was produced by over-expression of the corresponding cDNA.

The NMR spectra show that the substitution of K^+ ions by Na^+ increases considerably the Ca^{2+} affinity of site III resulting in a stable and persistent three-dimensional structure. Therefore, we decided to determine the solution structure of the Ca^{2+}-saturated LC-HCen2 domain, using NMR spectroscopy and molecular modeling.

^1H-^1H NOESY (Nuclear Overhauser Effect SpectroscopY) is useful for determining which signals arise from protons which are close in space but not closely connected by chemical bonds. A NOESY spectrum yields through space correlations *via* the Nuclear Overhauser Effect (NOE). When one multiplet is irradiated, the intensities of multiplets arising from nearby nuclei are affected. NOE is very sensitive to the distance and may therefore be used to estimate it. With enough measurements of this type, the conformation of a molecule in solution may be determined. The NOESY experiment also yields cross peaks arising from chemical exchange. If detecting exchange is the main purpose of the experiment it is refered to and EXSY (EXchange SpectroscopY). The most used NOESY pulse sequence is with a gradient homospoil. The homospoil supresses multiple quantum coherences so any COSY-type artifacts arise only from zero quantum coherence.

Proton resonance assignment of LC-HCen2 in Ca^{2+}-saturated state was done using the standard sequential assignment procedure, based on the identification of spin systems corresponding to amino acid residues, and their association to precise residues in the primary structure. The resonance peaks from residues between K96 and T102 remained unassigned, probably due to a slow exchange between several conformation in this fragment, resulting in very broad peaks. Combined analysis of secondary chemical shift of H^α protons (attached to the C^α from the polypeptide chain), and of short- and medium-range NOEs between backbone protons enabled to delineate the secondary structure elements along the sequence. The protein is mainly helical with five α-helices: F89-Q95, K103-F113, F123-E132, D139-A149, E159-K167 as can be concluded from Figures 1 and 2. Equally shown are the residues in the Ca^{2+} binding loops of the HCen3. The residues providing ligands to the metal ion are labeled by the letters corresponding to a Cartesian coordinate system, centered on Ca^{2+}. The elements of secondary structure of LC-HCen2, determined in the present work, are indicated under the sequences.

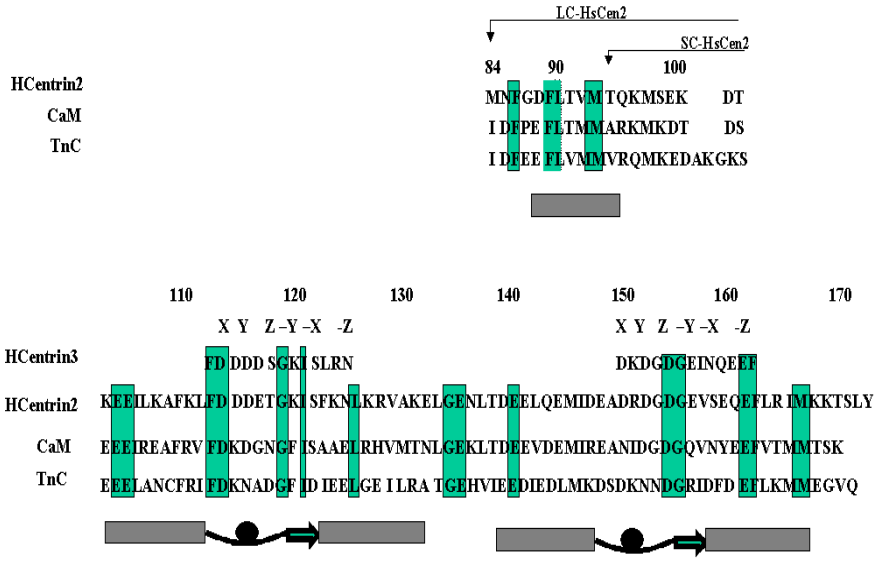

Fig. 1. Sequence comparison of LC-HCen2 with the corresponding fragments in CaM and TnC.

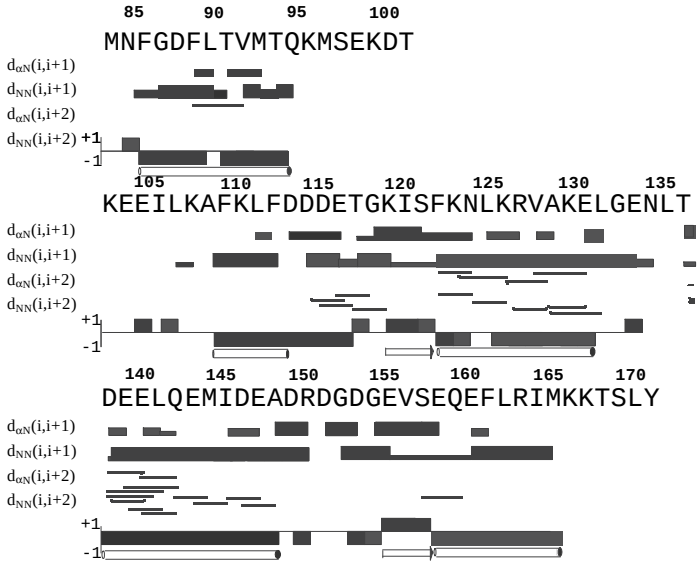

Fig. 2. Secondary chemical shifts and short- and medium-range NOE interactions between backbone protons along the sequence of LC-HCen2.

Additional information on the structure and dynamics of the helical elements was obtained from the study of exchange kinetics of amide protons. Detection of slowly exchanging amide protons in a α-helix indicates the participation of the corresponding protons in a hydrogen bond, typically of the type O(i)…H^N(i+4). The slowest exchanging protons correspond to the helix G (H^N(I42), H^N(I43) H^N(I44), H^N(I45) and H^N(I46)), suggesting that this is the most stable helix of the domain.

Two small strand antiparallel -β sheet fragments was identified due to the downfield shifted H^α protons ($4.2 < \delta < 5.2$) and the strong sequential NOE connectivities $d_{\alpha N}$ (i,i+1): K120-S122 and E156-S158. The strong dipolar interactions between H^α protons were observed on the two strands (H^α120/H^N159) (Fig. 3). Do to close chemical shift values, the connectivity H^α122/H^α156 (H^α120/H^α158), between H^N protons (H^N120/H^N157) and between H^N, H^α protons was not identified. The observed secondary structure elements of the LC-HCen2 domain are similar to those observed for other domains of the EF-hand family.

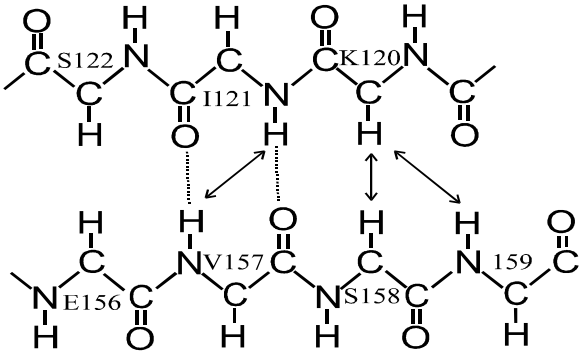

Fig. 3. NOE connectivities (arrows) between the two strands forming the anti-parallel β-sheet in LC-HCen2. The interrupted lines represent hydrogen bonds identified by the slow exchange of the corresponding amide protons.

According to its primary structure, the fourth Ca^{2+}-binding loop in HCen2, should have the highest binding affinity for the metal ion (Fig. 1). Within the EF-loop, positions 1, 3, 5, 7, 9 and 12 provide the critical residues that coordinate the bound ion [10]. The most critical substitution in the site III is the Asn residue in position –Z which is

usually a Glu residue [11]. The side chain in this position is able to give only one oxygen ligand (instead of two carboxyl oxygens in a Glu residue) to the metal ion. Therefore, the Ca^{2+} binding affinity of site III should be considerably lower.

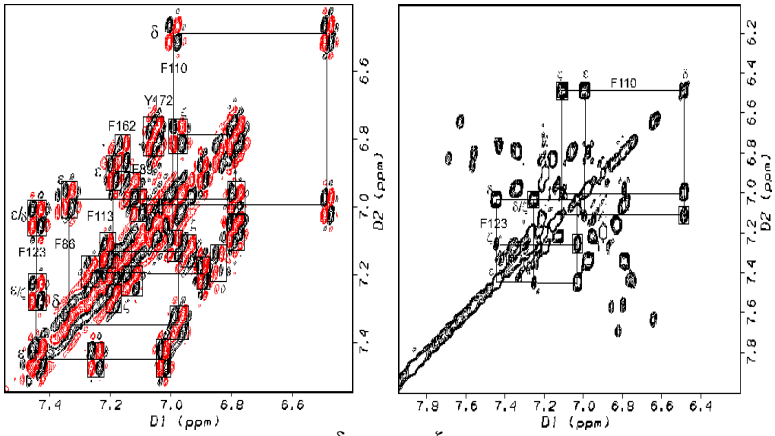

Fig. 4 .The aromatic protons (H^{δ}, H^{ε} ,H^{ζ}) assignment using 2D COSY and TOCSY spectra.

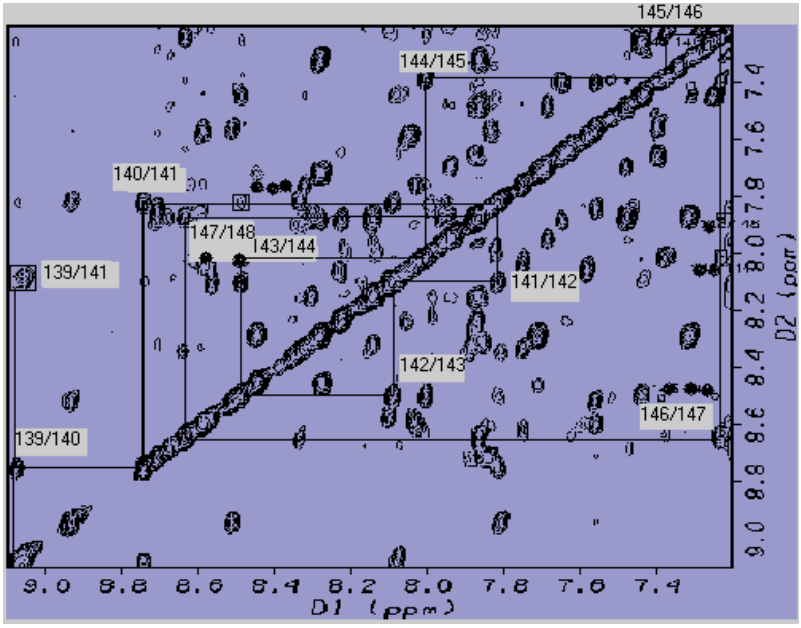

Fig. 5. LC-HCen2 -sequential assignment in the NH-NH region of NOESY spectra.

Another residue, which is highly conserved in the Ca^{2+}-binding loop of EF-hand proteins, is the Gly in position 6. Analysis of the high resolution structures indicates that the amide group of this residue is hydrogen-bonded to one of the carboxyl oxygen from Asp residue in position 1 [12]. In the NMR spectra this is reflected in a large downfield shift of the resonance corresponding to the Gly amide proton. In our experimental conditions, the chemical shift of the amide proton in G119 and G155 (position 6 in site III and site IV), are 10.95 and 9.90 ppm, respectively, strongly suggesting that the canonical hydrogen bond exists in both EF-hand motifs. The existence of the hydrogen bonds are also supported by observation of a slow H/D exchange rate for the corresponding amide protons.

The assignment of proton resonances was obtained using homonuclear and heteronuclear 2D and 3D NMR experiments.

The spin system was identified from COSY and TOCSY spectra recorded at 35 ºC. The primary structure analysis (Fig.1) shows the presence of six Phe and one Tyr. The spin system of these aromatic protons is given in Figure 4.

The proton sequential assignment of LC-HCen2 in saturated state, was obtained using a sequence-specific procedure [13] (Fig. 5).
A large number of long distance connectivities contributing to the global folding of the protein were observed for side chains of aromatic protons.

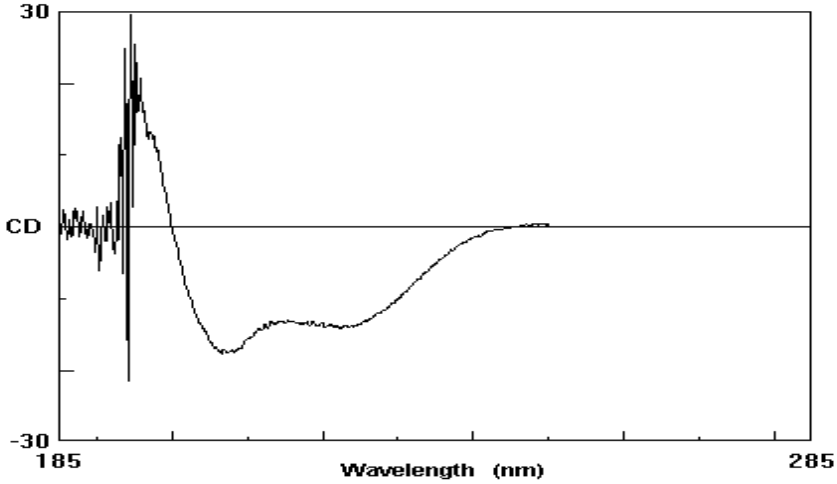

Fig. 6. UV-far DC spectra of 112µM HCen2, Tris 1mM, 100mM KCl, pH=7.6, recorded at 25º C.

The far-UV spectra recorded at room temperature are presented in Figure 6. By analogy with standard DC spectra one remarks that the human centrin 2 shows mostly two structural type: α helix and β-sheet. To estimate the percentage of α helix we have used an empirical method based on the calculation of the ratios between the ellipticity value measured at 222 nm for the protein and the ellipticity at the same wave length that was found for a 100 % α helix twenty residues peptide. Analysis of the spectra using a program for secondary structure prediction [14] indicates that there is 22% α helix in "apo" form and 30% in the presence of Ca^{2+} binding ions and 3% β-sheet .

The chemical stability of investigated samples was estimated using an induced unfolding process. Urea-induced unfolding process of human centrin 2 and of the two C-terminal fragments, LC-HCen2 and Sc-HCen2, was monitored by the change of the ellipticity at 222 nm, at pH 7.6, in function of concentration of denaturant (0-8 mM uree). The protein concentration was adjusted to 0.2 μM for the integral protein, 11.3 μM for the long fragment LC-HCen2 and 13.1 μM for the shorter fragment Sc-HCen2, in Tris buffer (10 mM), KCl (10 mM). The samples in presence of $CaCl_2$ 1mM, were incubated until equilibrium was reached at the temperature chosen for determining the unfolding curve (25 °C).

The curves of urea unfolding of "apo" and Ca^{2+}- HCen2, LC-HCen2 and SC-HCen2 form, were analyzed by the linear extrapolation method. The Gibbs free energy of unfolding (ΔG^0) is given by the equation:

$$\Delta G^0 = - RT\ln K \qquad (1)$$

where K is the equilibrium constant of unfolding at a given temperature, $K= f_u/f_n$, f_n is the native protein fraction and f_u is the unfolding protein fraction ($f_u = 1- f_n$). In the chemical denaturation experiments the free energy difference is a linear function [15] of the denaturant concentration that can be written:

$$\Delta G^0 = \Delta G^0_{H_2O} - m[dnt] \qquad (2)$$

where $\Delta G^{0}_{H_2O}$ is the free energy in absence of the denaturant, [dnt] is the denaturant concentration and m is a parameter to be determined.

$$\Delta G^{0}_{H_2O} - m[dnt] = - RT \ln \frac{f_u}{1-f_u} \quad (3)$$

The best values of the $\Delta G^{0}_{H_2O}$ and m parameter were chosen to fit the experimental data (Fig. 7) according with the relationship :

$$f_u = [\exp(m[dnt] - \Delta G^{0}_{H_2O})/RT]/ [1+\exp(m[dnt] - \Delta G^{0}_{H_2O})/RT] \quad (4)$$

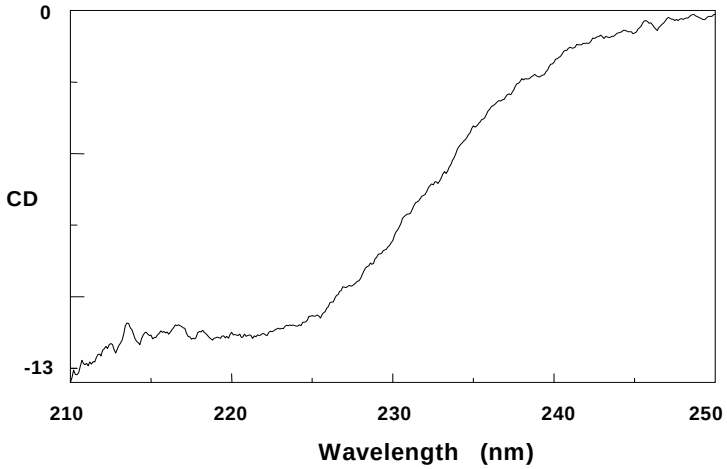

Fig. 7.The chemical HCen2 denaturation CD spectra recorded at 25°C for a denaturant concentration of 0.5 M.

The unfolding profile curve shows two distinct steps, corresponding to N-terminal and C-terminal denaturation process, with different values for the midpoint concentration (C_m are 1.4 M and 4.3 M). The two halves of HCen2 have different structural stability. Further, the shorter fragment's unfolding curve shows a single step transition with C_m of 3.8 M values close to the value of the second step of the integral protein. Therefore the N-terminal domain, which represents the first unfolding unit, has a lower stability, similar to that of the EF-hand domains in Ca^{2+}-free CaM [16].

Conclusions

The NMR studies reveal that human centrin 2 is member of Ca^{2+}-binding protein which has two EF-hand motifs in the C-terminal domain. Unlike to the SC-HCen2 domain characterized by a significant structural flexibility, the LC-HCen2 obtained by proteolysis process exhibits a pronounced structural stability. The presence of Gly in position 6 of the Ca^{2+}-binding loop, reflected in a downfield shift of the resonance corresponding to the amide proton shows that this is a very conserved and inherent residue in the EF-hand motif structural stability.

The far-UV DC experiments allowed us to evaluate the percentage of secondary structure of type helix present in the protein. Analysis of the spectra indicates that there is 22% α helix in "apo" form and 30% in the presence of Ca^{2+} binding ions and 3% β-sheet .

The results obtained by chemical denaturation indicate that the LC-HCen2 long domain has a more pronounced structural stability then the SC-HCen2 short domain. Also N- terminal domain has a lower structural stability due to a low affinity of the Ca^{2+} binding.

REFERENCES

1. Brinkley, B. R., Annu. Rev. Cell Biol. 1, 145-172, 1985.
2. Mazia, D., Int. Rev.. Cytol. 100, 49-92, 1987.
3. M.W.G. de Bolster, Bioinorganic Chemistry, IUPAC Recommen-dations, 1997
4. Babu, Y.S., Bugg, C.E. and Cook, W.J., J.Mol. Biol., 204, 191-204, 1988.
5. Durussel, I., Blouquit, Y., Middendorp, S., Craescu, C.T., and Cox, J.A., FEBS, Lett. 472, 208-212, 2000.
6. Finn, B.E., Evenas, J., Drakenberg, T., Waltho, J.P., Thulin, E., and Forsen, S., Nat. Struct. Biol., 2, 777-783, 1995
7. Slupsky, C.M., and Sykes, B.D., Biochemistry 34, 15953-15964, 1995
8. Spyracopoulus, L., Li, M. X., Sia, S. K., Gagne, S.M., Chandra, M., Solaro, R.J., and Sykes, B.D., Biochemistry 36, 12138-12146, 1997
9. Gagne, S. M., Tsuda, S., Li, M. X., Smilie, L.B., and Sykes, B.D., Nat. Struct. Biol. 2, 784-789, 1995.
10. J. J. Falke, S. K. Drake, A. L. Hazard and O.B. Peersen, Quartely Reviwes of Biophysics, 27, 219-290, 1994
11. Reid, R. E., J. Biol. Chem., 265, 5971-5976, 1990.
12. Krudy, G.A, Brito, R. M. M., Putkey, J. A., and Rosevear, P.R., Biochemistry 31, 1595-1602, 1992
13. Wüthrich, K. NMR of proteins and nucleic acids. (Wiley, New York), 1986.
14. Johnson, W.C., Proteins, 35, 307-312, 1999
15. Pace, C.N. Methods Enzymol. *131*, 266-280., 1986.
16. Masino, L., Martin, S.R., and Bayley, P.M. Prot. Sci. 9, 1519-1529, 2000.

STUDIA UNIVERSITATIS BABEŞ-BOLYAI, PHISICA, XLXVIII, 2, 2003

A METHOD FOR SULFUR ISOTOPES DETERMINATION FROM MINERAL SULPHUROUS WATERS

STELA CUNA[1], GABRIELA MURESAN[1], ONUC COZAR[2]

ABSTRACT. Sulfur isotopic ratio in terrestrial and aquatic samples varies because of an isotopic fractionation by geological and biological process. Sulfur fractionation of mineral sulphurous water offers information about their sources, some biological process from past, relationship between hydrocarbon deposits and mineral sulphurous waters. Thus, for such studies we have elaborated a method for determination of sulfur isotopes from mineral sulphurous water. We have reported measurements for 22 samples. The results were obtained with a precision of ±0.1‰ for n=5.

INTRODUCTION

Sulfur is widely distributed in the lithosphere, biosphere, hydrosphere and atmosphere of the Earth. It occurs in the oxidized form as sulfate in the oceans and in evaporates rocks. It is found in the native state in the cape rock of salt domes and in the rocks of certain volcanic regions. Sulfur also occurs in the reduced form as sulfide in metallic mineral deposits associated with sedimentary and metamorphic rocks.

Sulfur has four stable isotopes: ^{32}S, ^{33}S, ^{34}S, ^{36}S with the abundance 95.02 %, 0.75 %, 4.21 % and respectively 0.02 %.

Stable isotopic ratios of sample are reported in parts per thousand relative to a standard, according to the following equation [3, 4, 7]:

$$\delta^{34}S = \left[\frac{\left(^{34}S/^{32}S\right)_{spl} - \left(^{34}S/^{32}S\right)_{std}}{\left(^{34}S/^{32}S\right)_{std}} \right] x10^{3}‰$$

Sulfur isotopic data are reported to the sulfur in troilite (FeS) of the iron meteorite Canyon Diablo whose $^{32}S/^{34}S$ ratio is 22.22. Because troilite of iron meteorites is isotopically uniform, samples from Canyon Diablo are used as standard defining the zero point of the $\delta^{34}S$ scale.

The purpose of this study is to elaborate the measurement method of ^{34}S from H_2S dissolved in mineral waters. Sulfur fractionations of mineral sulfurous waters offers informations about their sources, some biological process from past, relationship between hydrocarbon deposits and mineral sulfurous waters. Thus, for such studies was necessary to elaborate a method for determination of sulfur isotopes from mineral sulfurous water.

Mineral waters are distinguished of ordinary waters either the concentrations or the composition or both of them. Local conditions have an important role for the production of these differences.

The most important cause for variations in the isotopic composition of sulfur in nature is the reduction of sulfate ions by anaerobic bacteria such as *Desulfovibrio* which live in sediment deposited in the oceans and in lakes. This bacterium splits oxygen from sulfate ions and excreted H_2S that is enriched in ^{32}S relative to the sulfate. The extent of fractionation is variable and depends on certain rate-controlling steps in the reactions by which the sulfur is metabolized.

SAMPLES PREPARATION

The isotopic analysis of sulfur requires the production of a suitable gaseous compound of the element that can be introduced into the source region of a gas source mass spectrometer. The normal gas used for sulfur isotope analysis is sulfur dioxide, SO_2 [1,2].

For this experimental method we are interested in dissolved sulfates water and H_2S.

First step for sulfur isotopic analysis from dissolved sulfates and H_2S is the sample preparation. The techniques of preparation must be accomplished the following three conditions:

-it is necessary that SO_2 to be pure,
-don't produce isotopic fractionation during preparation process,
-the SO_2 quantity must be enough for analysis.

To obtain the sulfur dioxide from H_2S from mineral water, we have built a special installation for convert cadmium sulfide to silver sulfide.

The typical procedure is:

-H_2S from mineral waters is absorbed in a cadmium acetate solution resulting CdS,

- -filter, wash and dry the CdS,
- -add HCl resulting H_2S

$$CdS+2HCl \rightarrow H_2S+CdCl_2$$

- -H_2S is passing in a stream of nitrogen in a silver nitrate solution and it is
- precipitated as Ag_2S

$$H_2S+2AgNO_3 \rightarrow Ag_2S+2HNO_3$$

- -than Ag_2S is passing in a stream of oxygen at 1100^0C resulting SO_2

$$2CuO \rightarrow Cu_2O+1/2O_2$$
$$2Ag_2S+3O_2 \rightarrow 2Ag_2O+2SO_2$$

THE MASS SPECTROMETRIC ANALYSIS OF SULFUR

The determination of isotopic abundance in the range of natural concentration must be made with great precision because of very small variation of this abundance relative to normal value [5]. Using double inlet system and comparing the sample with a standard, we eliminate systematic errors and double collector measurements of isotopic ratio can eliminate the accidentally errors.

The mass spectrometer used in this study is an ATLAS M 86.

The covered stages, for determination of sulfur's natural abundance, are:

- -determination of relative values of natural isotopic abundance $\delta^{64}S$ and
- $\delta^{66}S$ by mass spectrometer
- -the assessment and application of corrections at this measurements
- -to report δ values at CDT standard.

RESULTS. CONCLUSIONS

The results of sulfur isotopic measurements from 22 sample of different mineral waters are listed in Table 1. The number of the measurements for each sample was 3.

Table 1

Sample	$\delta^{34}S$ vs. CDT ‰	$R=^{32}S/^{34}S$	Observations of sulfur origin from mineral waters
0	1	2	3
Spring 1	+27.21	21.63	Dissolved sulfates in mineral waters or mineral deposits as sulfates
Spring 2	-8.38	22.41	Hydrogen sulfide of biogenic nature
Spring 3	-10.42	22.45	Hydrogen sulfide of biogenic nature
Spring 4	+2.64	22.16	Native sulfur from sediment origin
Spring 5	+22.81	21.72	Deposited sulfides and water dissolved sulfates
Spring 6	-30.01	22.90	Deposited sulfides
Spring 7	-20.34	22.68	Native sulfur of biogenic nature or Hydrogen sulfide of biogenic nature or deposited sulfides
Spring 8	-18.98	22.65	Native sulfur of biogenic nature or Hydrogen sulfide of biogenic nature or deposited sulfides
Spring 9	-18.69	22.64	Native sulfur of biogenic nature or Hydrogen sulfide of biogenic nature or deposited sulfides
Spring 10	-15.09	22.56	Native sulfur of biogenic nature or Hydrogen sulfide of biogenic nature or deposited sulfides
0	1	2	3
Spring 11	-4.42	22.32	Hydrogen sulfide of biogenic nature or deposited sulfides
Spring 12	+4.63	22.11	Sulfides from volcanic emanation, native sulfur from deposited origin, deposited sulfides and sulfates
Spring 13	-34.59	23.01	Deposited sulfides
Spring 14	-25.88	22.81	Deposited sulfides
Spring 15	-46.49	23.30	Deposited sulfides
Spring 16	+8.74	22.02	Deposited sulfates, native sulfur from deposited origin
Spring 17	-7.73	22.39	Deposited sulfides

Spring 18	+4.24	22.12	Sulfides from volcanic emanation, native sulfur from deposited nature, deposited sulfides and sulfates
Spring 19	+8.72	22.03	Deposited sulfates, native sulfur from deposited origin and volcanic nature
Spring 20	+3.78	22.13	Deposited sulfates, native sulfur from deposited origin and volcanic nature
Spring 21	+4.09	22.13	Deposited sulfates, native sulfur from deposited origin and volcanic nature
Spring 22	+23.25	21.17	Deposited sulfates, native sulfur from deposited origin and volcanic nature

We developed a method for sulfur isotopes determination from mineral sulphurous water. The sample preparation technique is based on an installation for convert CdS to Ag_2S and a vacuum extraction line for combustion of Ag_2S and cryogenic purification of resulted SO_2.

Isotopic analyses were performed by using an isotope ratio mass spectrometer. The precision of the measurements was ±0.1‰.

We have used the $\delta^{34}S$ values to determine the origin of sulfur such as: dissolved sulfates in mineral waters or mineral deposits as sulfates, hydrogen sulfide of biogenic nature, native sulfur from sediment origin, sulfides from volcanic emanation, etc.

The obtained data are in good agreement with the literature [3, 4, 6].

REFERENCES

1. Carmody, Rebecca, Plummer, L.N., Busenberg, E., and Coplen, T.B., (1998) *Methods for collection of dissolved sulfate and sulfide and analysis of their sulfur isotopic composition*, U.S. Geological Survey, Reston, Virginia
2. Coleman, M.L., and Moore, M.P. (1978), *Direct reduction of sulfates to sulfur dioxide for isotopic analysis*, Anal. Chem., 50, 1594-5.
3. Glesemann, A., Jager, H.-J., Norman, A.L., Krouse, H.R. and Brand, W.A. (1994), *On-line sulfur isotope determination using an elemental analyzer coupled to a mass spectrometer,* Anal. Chem., 66, pp. 2816-2819
4. Mayer, B., Fritz, P., Prietzel, J. and Krouse, H.R. (1995), *The use of stable sulfur and axygen isotope ratio for interpreting the mobility of sulfate in aerobic forest soils,* Applied Geochemistry, vol. 10, pp. 161-173
5. Rees, C.E., Holt, B.D., *The Isotopic Analysis of Sulphur and Oxygen in "Stable Isotopes in the Assessment of Natural and Anthropogenic Sulphur in the Environment*", 1991 SCOPE, Published by John Wiley & Sons Ltd.
6. Toran, L., (1987), *Sulfate contamination in groundwater from a carbonate-hosted mine,* J. Contam. Hydrol. 2, 1-29
7. Wong, W.W., Ho, W.-K., Brewer, R.L. and Kaplan, I.R. (1985), *Stable isotope composition of sulfates in aerosol particles collected in the southern California Air Basin,* Int. J. Appl. Radiat., vol. 36, no. 12, pp. 947-951

STUDIA UNIVERSITATIS BABEŞ-BOLYAI, PHISICA, XLXVIII,2 2003

STRUCTURAL STABILITY OF SOME PHOSPHATE GLASSES

S. SIMON, DANA CACAINA, I. BALASZ

Faculty of Physics, Babes-Bolyai University,
3400 Cluj-Napoca, Romania

ABSTRACT. Glasses of x $(Nb_2O_5 \cdot Li_2O)(100\text{-}x)[P_2O_5 \cdot CaO]$ system with $0 \leq x \leq 20$ mol % were investigated by differential thermal analysis (DTA). Thermal differential data obtained at different heating rate were used to determine the activation energy of crystallisation (E_t), while the thermal stability was appreciated at same heating rate for all samples. DTA results lead to close values for the activation energy for both x = 1 and 5 mol % and a clearly higher value for x = 3 mol %. The highest glass stability was also obtained for x = 3 mol % and decreases by further addition of Nb_2O_5 and Li_2O up to x = 20 mol %.

Introduction

Recently there has been a large interest on improving the physical properties and the chemical durability of phosphate glasses by introducing several glass formers and modifiers into P_2O_5 glass network[1-3]. These additives can confer high thermal expansion coefficients, good optical properties and reasonable chemical durability to phosphate glass matrices. Phosphate glasses and ceramics are of technological interest for electrochemistry devices, in electronic industry but also as bioactive materials[4].

The aim of this study is to investigate crystallisation possibilities of niobium lithium calcium phosphate glasses by differential thermal analysis, important for the controlled development of $LiNbO_3$ phase in vitroceramics obtained by heat treatment from these precursor glasses.

Experimental

The investigated glass system $x(Nb_2O_5 \cdot Li_2O)(100-x)[P_2O_5 \cdot CaO]$ was prepared in the composition range $0 \leq x \leq 20$ mol % using as starting materials reagent grade chemicals Nb_2O_5, Li_2CO_3, $CaCO_3$ and $NH_4H_2PO_4$. The homogenised mixtures were melted at 1200^oC for 10 minutes in sintered corundum crucibles in an electric furnace and then the melts were quickly undercooled at room temperature by pouring onto stainless steal plates.

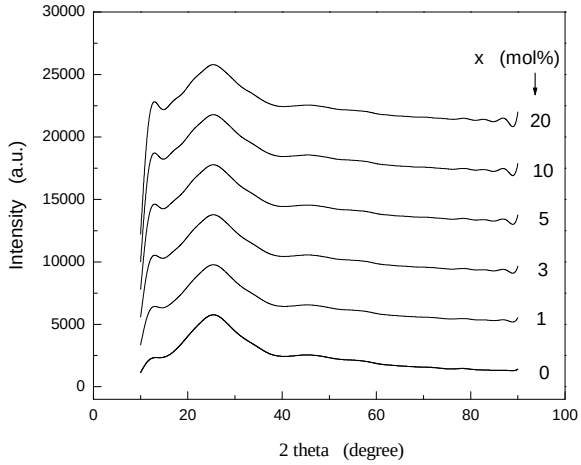

Fig.1. X-ray diffraction patterns for $x(Nb_2O_5 \cdot Li_2O)(100-x)[P_2O_5 \cdot CaO]$ glass samples.

The vitreous structure of the samples was confirmed by X-ray powde

r diffraction carried out at room temperature (Fig. 1) with a Bruker spectrometer system. The glass transition temperatures (T_g) and crystallisation temperatures (T_{cr}) of the samples have been determined in the temperature range 20-1000^0C by using a MOM equipment. A uniform heating rate of 10^oC/min was employed for this purpose. The activation energy of the crystallisation (E_t) for different heating rate a = 5, 10 and 20^0C/min was evaluated according to Kissinger's equation[5].

Results and discussion

DTA curves recorded with the same heating rate of 10°C/min for all investigated glasses are illustrated in Figure 2. Thermogravimetric and differential thermogravimetric curves show that there are no weight losses for these samples. One remarks that the glass transition temperature corresponding to the matrix sample (x = 0) is diminished by addition of $Nb_2O_5 \cdot Li_2O$. Following the T_g values for the samples containing Nb_2O_5 and Li_2O one observes a weakly higher value for x = 3 mol %. On the other hand, the glass transition temperature decreases by further addition of Nb_2O_5 and Li_2O to glass matrix, as can be seen from Figure 3. The value of T_g for samples containing between 3 and 10 mol % ($Nb_2O_5 \cdot Li_2O$) decreases from 575 to 550°C, while for the samples with $10 \leq x \leq 20$ mol % the glass transition temperature is practically unchanged. This composition dependence of T_g suggests[6] that a structural change could occur at x =10 mol % ($Nb_2O_5 \cdot Li_2O$).

An exothermic peak at 760°C corresponding to a crystallisation process (T_{cr}) is evidenced in the DTA curve of the matrix sample. This peak appears from all samples, but at shifted temperature. In addition to the peak observed at 715°C for x = 1 mol % and at 745°C for x = 3 mol %, the DTA traces of these samples show weaker exothermic events around 635°C and 680°C. For the samples corresponding to the compositions x = 5, 10 and 20 mol % is prevalent the exothermic peak recorded in the range 690 - 710°C (T_{cr}). As can be observed from Table 1, the crystallisation temperature decreases with increasing concentration of ($Nb_2O_5 \cdot Li_2O$), excepting the sample with x = 3.

For the samples without or with low niobium and lithium content ($x \leq 5$ mol %) the exothermic peak T_{cr} is followed by an endothermic event between 900 and 1000°C, that could be assigned to the melting of the glass. Up to 1000°C this endothermic effect is not occurring for $x \geq 10$ mol %. It is to bring up that the system was prepared by undercooling from 1200°C, that allowed to obtain glass samples also for these compositions. And. The melting of the samples would be pointed out by an endothermic event in the DTA traces if the differential thermal analysis runs are not limited at 1000°C like in this experiment.

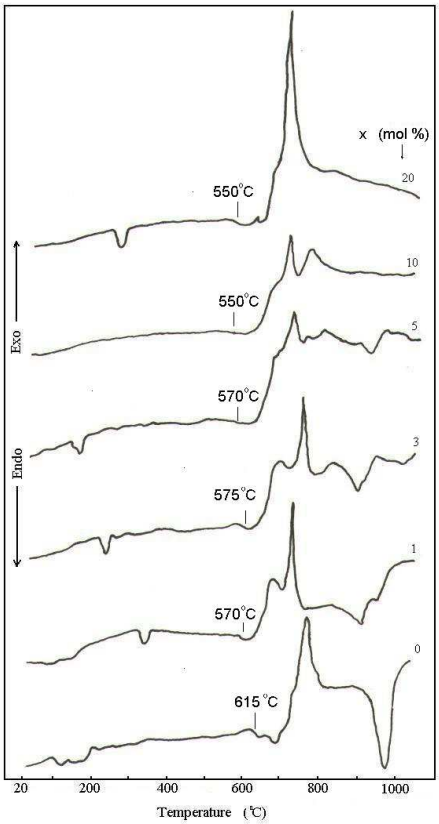

Fig. 2. Differential thermal analysis curves of $x(Nb_2O_5 \cdot Li_2O)(100-x)[P_2O_5 \cdot CaO]$ samples.

For different heating rate, *a* (a = 5, 10, 20 degree/min), the activation energy of crystallisation was discussed according to Kissinger's formula[5], as given by equation:

$$\ln\left(T_{cr}^2/a\right) = E_t/RT_{cr} + \text{const.} \quad (1)$$

where T_{cr} is a temperature corresponding to the maximum of the DTA crystallisation peak, E_t is the effective activation energy of crystallisation and R is the gas constant.

Table 1

Activation energy of crystallisation (E_t), glass transition temperature (T_g), crystallisation temperature (T_{cr}), glass stability S, K_{gl}, S/T_g, T_g/T_m and S/T_m for $x(Nb_2O_5 \cdot Li_2O)(100-x)[P_2O_5 \cdot CaO]$ samples.

X (MOL %)	T_G ^OC	T_{CR} ^OC	S ^OC	S/T_G	T_G/T_M	S/T_M	K_{GL}	E_T KJ/MOL
0	615	760	145	0.24	0.81	0.15	0.7	
1	570	715	145	0.25	0.80	0.16	0.7	94.73
3	575	745	170	0.30	0.77	0.19	1	128.81
5	570	710	140	0.25	0.80	0.15	0.6	96.40
10	550	700	150	0.27				
20	548	690	142	0.26				

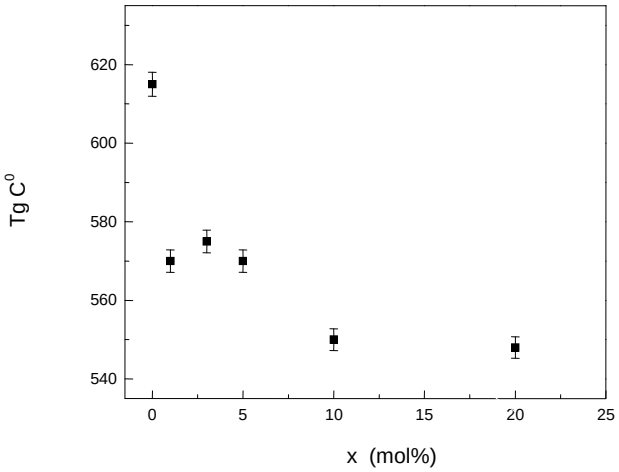

Fig.3. Composition dependence of glass transition temperature.

Figure 4 shows the plots of $\ln(T_{cr}^2/a)$ versus the reciprocal crystallisation temperature, T_{cr}^{-1}, for different heating rates. The activation energy for crystallisation (E_t) was calculated from a linear fitting of Kissinger's equation.

The glass stability can be expressed[7,8] by the difference of crystallisation and glass transition temperatures, $S = \Delta T = T_{cr}-T_g$. Larger values of ΔT lead to higher thermal stability of the glasses. The glass stability can be also expressed also by parameters like the

Hruby parameter, $K_{gl}=(T_{cr}-T_g)/(T_m - T_{cr})$ [13], or the ratios $(T_{cr}-T_g)/T_g$, T_g/T_m, $(T_{cr}-T_g)/T_m$ [1]. Figure 5 illustrates different stability parameters for the investigated glasses.In Table 1 are summarised glass transition and crystallisation temperatures as well as the calculated values of activation energy of crystallisation and stability parameters. Inspecting these data one remarks that the glass with 3 mol % $Nb_2O_5 \cdot Li_2O$ has the highest thermal stability as indicated by almost all glass stability parameters.

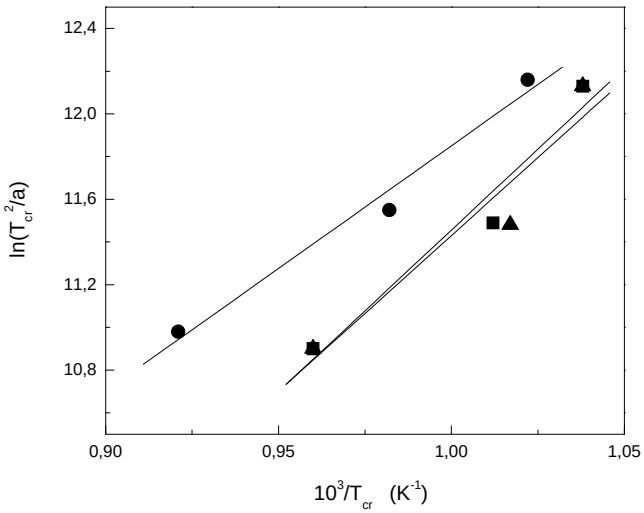

Fig.4. Plot of $\ln(T_{cr}^2/a)$ versus $10^3/T_{cr}$ of the samples with x = 1 mol % (■), 3 mol % (●) and 5 mol % (▲).

The activation energy for crystallisation (E_t) was explored for the samples with $1 \leq x \leq 5$ mol %. One observes that E_t changes with $Nb_2O_5 \cdot Li_2O$ content and ranges from 94.7 to 128.8 kJ/mol in this composition range and has the same behaviour as the glass stability, i.e. a maxim value for x = 3 mol % glass sample (Fig. 6). This composition dependence of the activation energy of crystallisation with respect to introduction of $(Nb_2O_5 \cdot Li_2O)$ in the network of calcium phosphate glass matrix could be attributed to the creation of non-bridging oxygens which needs more energy for breaking the bonds in

the network. It is known[9, 10] that vitreous P_2O_5 consist in a polymeric structure of PO_4 units, where phosphorous is four coordinated and only three of the oxygen atoms of each unit bridge to neighbouring units, while the forth is doubly bonded to the central phosphorous atom. The addition of the modifier leads to a depolymerisation of the network with oxygen breaking the P-O-P links by converting bridging oxygens to non-bridging oxygens[11]. The MAS NMR studies[10,12] of these glasses show that the addition of Nb_2O_5 and Li_2O to $[P_2O_5 \cdot CaO]$ matrix depolymerises the network structure. These results are in agreement with the data obtained from the differential thermal analysis carried out in this study.

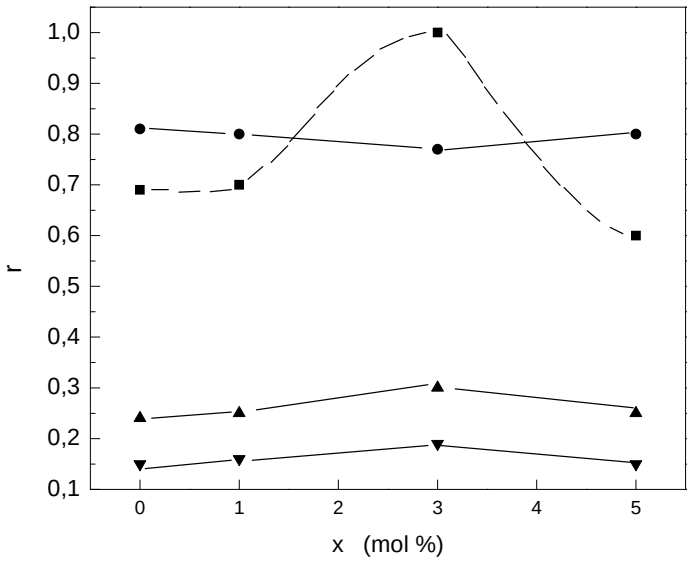

Fig. 5. Composition dependence of glass stability parameters expressed by the ratios K_{gl} (■),$S/T_{g,}$ (▲), T_g/T_m (●) and S/T_m (▼) for $x(Nb_2O_5 \cdot Li_2O)(100\text{-}x)[P_2O_5 \cdot CaO]$.

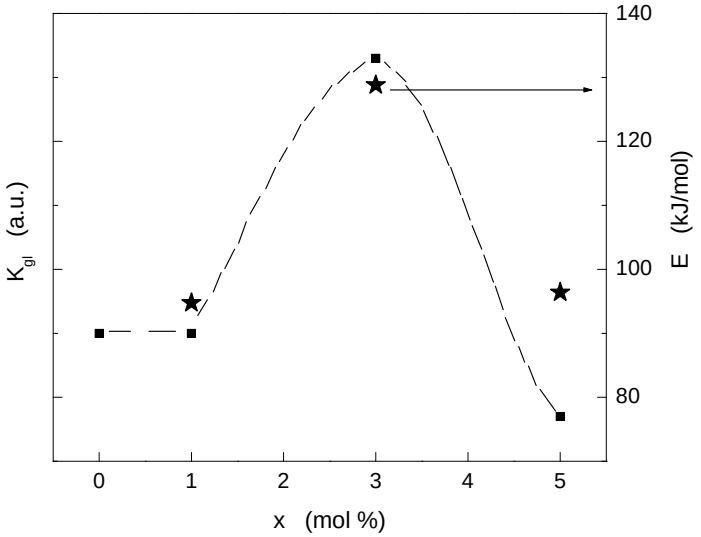

Fig. 6. Composition dependence of K_{gl} parameter and activation energy of crystallisation for $x(Nb_2O_5 \cdot Li_2O)(100\text{-}x)[P_2O_5 \cdot CaO]$ glasses with $0 \leq x \leq 5$ mol %.

Conclusions

Glass samples belonging to $x(Nb_2O_5 \cdot Li_2O)$ $(100\text{-}x)[P_2O_5 \cdot CaO]$ system ($0 \leq x \leq 20$ mol %) have been prepared and tested by X-ray diffraction and differential thermal analysis in order to study the effect of the increasing of $Nb_2O_5 \cdot Li_2O$ content on $P_2O_5 \cdot CaO$ glass matrix stability. The glass transition and crystallisation temperatures are lower for the samples containing $Nb_2O_5 \cdot Li_2O$ than for glass matrix and decrease as $x > 3$ mol %**.** The dependence of glass stability on $Nb_2O_5 \cdot Li_2O$ content point out a relative maximum for $x = 3$ mol %.

The values calculated for the activation energy are ranging from 94.7 to 128.8 kJ/mol and follow a similar composition dependence with that of glass stability parameters.

REFERENCES

1. P. Subbalakshmi; N. Veeraiah, J.Non-Cryst.Solids, 298, 8 (2002)
2. E. Rashid; B.L. Phillips, S.H. Risbud, J.Mater.Res., 15, 11, 2463 (2000).
3. L. Montagne; G. Palavit, Phys.Chem.Glasses, 38, 15 (1997).
4. Y. Zhang, J.D. Santos, J.Non-Cryst.Solids. 272 14, (2000).
5. H. Kissinger, J.Res. Nat. Bur. Stand, 57, 217 (1956).
6. A. Pan, A. Ghosh, J.Non-Cryst.Solids. 271, 157 (2000).
7. E.B. Arauj, J.A. Eiras, E.F. de Almeida, J.A.C. de Paiva, A.S.B. Sombra, Phys.Chem.Glasses, 40, 5, 273 (1999).
8. R. El-Mallawany, Proc.Int.Congr.Glass,Volume 2. Extended Abstracts, Edinburg, Scotland, 1-6 July 2001.
9. R.K. Brow, D.R. Tallant, J.J. Hudgens, S.W. Martin, A.D. Irwin, J.Non-Cryst. Solids,177, 221 (1994).
10. R.K. Brow, D.R. Tallant, T. Myers, C.C. Phifer, J.Non-Cryst.Solids. 191, 45 (1995).
11. U. Hoppe, J.Non-Cryst.Solids. 195, 138 (1996).
12. S. Simon, D. Cacaina, M. Vasilescu, V.R.F. Turcu, National Biomaterials Symposium, Bucharest, 13-14 dec. 2002.
13. A. A. Jr. Cabral, C. Fredericci, E. D. Zanotto, Non-Cryst. Solids, 219, 182 (1997).

STUDIA UNIVERSITATIS BABEŞ-BOLYAI, PHISICA, XLXVIIII, 2, 2003

CONTRIBUTIONS TO THE ULTRASONIC STUDY OF INTERNAL PRESSURE IN ALCOHOL - CARBON TERTRACHLORIDE MIXTURES

I. LENART[1], A. CIUPE[1]

ABSTRACT. The correlation of the different internal pressure formulas by means of the ultrasonic propagation velocity as a common parameter allowed us to establish the correction factors with respect to the rigorous expression of the internal pressure in liquids. The presented relations were verified in the case of the liquid binary systems: carbon tetrachloride - propilic alcohol, carbon tetrachloride - butylic alcohol and carbon tetrachloride - amilic alcohol in the temperature range 10 ÷ 40^0 C. For this purpose it were used the measured values of the ultrasonic propagation velocity, density and molar heat.

The internal pressure has different expressions owing either to the use of various models, or to the introduction of some approximations. That is reflected by the discrepancy of obtained values [1,2].

In order to establish the correction coefficients with respect to the rigorous internal pressure formula, the different relations have to be correlated by means of the mechanisms associated with the volume changes of the medium. To the volume changes that are dependent on the intermolecular forces corresponds internal potential energy changes.

The internal pressure, defined by:

$$p_i = \left(\frac{\partial U}{\partial V}\right)_T , \qquad (1)$$

results from the contribution of all the attractive and repulsive potentials [3]. It can be expressed as a function of the state parameters by:

[1] Faculty of Physics, "Babeş-Bolyai" University, Cluj-Napoca, Romania

$$p_i = T\left(\frac{\partial p}{\partial T}\right)_V - p \tag{2}$$

where p is the external pressure, which can be neglected in the case of liquids, excepting those subjected to high pressures.

After performing some changes on obtains the following formulas to calculate the internal pressure from experimental data:

$$p_i = \frac{\alpha T \rho c_s^2}{\gamma} \tag{3}$$

respectively:

$$p_i = \frac{\alpha T \rho c_s^2 C_p}{C_p + T\alpha^2 M c_s^2} \tag{4}$$

where: α is the volume expansion coefficient at constant pressure, T is the absolute temperature, ρ is the density, γ is the adiabatic exponent, c_s is the adiabatic ultrasound propagation velocity and M is the molar mass.

The van der Waals' internal pressure was obtained by making some approximations based on a simplified model in which the intermolecular interactions are limited to that of attraction by dispersion forces. Thus, expressing the potential component of the internal energy U corresponding to all pairs from a number N of molecules by:

$$U = -\frac{2}{3}\pi N^2 \frac{A}{r_0^3} \cdot \frac{1}{V} = -\frac{a}{V} \tag{5}$$

from (1) the van der Waals' internal pressure formula is obtained:

$$p_{iw} = \frac{a}{V^2} \tag{6}$$

where a is a constant and V is the molar volume.

With a view to get the relation between the real internal pressure p_i deduced by thermodynamic reasons and the van der Waals' internal pressure p_{iw}, it is necessary to express p_{iw} as a function of the ultrasound propagation velocity c_s that is defined by:

$$c_s^2 = \gamma\left(\frac{\partial p}{\partial \rho}\right)_T . \tag{7}$$

From (6) and (7) it results:

$$p_{iw} = \frac{\rho c_s^2}{2\gamma} \tag{8}$$

and from (3) and (8) we get the relation we sought for:

$$\mathrm{p_i} = 2\alpha \mathrm{T} \mathrm{p_{iw}} \tag{9}$$

where $2\alpha T$ represents the correction coefficient of the van der Waals' internal pressure.

A different method to evaluate the correction is possible by introducing of a parameter in the formula for the internal energy [4 ÷ 6]:

$$\mathrm{U} = -\frac{\mathrm{a}}{\mathrm{V}^{\mathrm{n}}} \tag{10}$$

whence:

$$\mathrm{p_i} = \left(\frac{\partial \mathrm{U}}{\partial \mathrm{V}}\right)_{\mathrm{T}} = \frac{\mathrm{an}}{\mathrm{V}^{\mathrm{n+1}}} \tag{11}$$

where n is a characteristic constant of the liquid, temperature dependent, and which for n = 1 corresponds to the van der Waals' condition.

The formulas (6), (9) and (11) allow a comparison of the two corrections:

$$\frac{\mathrm{an}}{\mathrm{V}^{\mathrm{n+1}}} = 2\alpha \mathrm{T} \frac{\mathrm{a}}{\mathrm{V}^2} \tag{12}$$

whence:

$$\frac{\mathrm{n}}{\mathrm{V}^{\mathrm{n+1}}} = 2\alpha \mathrm{T} \ . \tag{13}$$

In the van der Waals' definition of internal pressure (6) it is possible to introduce a rectified constant:

$$\mathrm{a_c} = \mathrm{a} 2\alpha \mathrm{T} \tag{14}$$

and thus:

$$p_i = \frac{a_c}{V^2} \tag{15}$$

where a_c is a constant characteristic of the liquid, being independent on the temperature at constant atmospheric pressure.

In order to calculate the internal pressures and the corresponding correction coefficients the following liquid systems were studied: carbon tetrachloride - propilic alcohol, carbon tetrachloride - butylic alcohol and carbon tetrachloride - amilic alcohol as well as the corresponding pure components. Measurements were performed for various concentrations in the temperature range $10 \div 40^0$ C.

Table 1a

(carbon tetrachloride – propilic alcohol system)

$\chi_{ALCOHOL}$	T[K]	$P_{IW} \cdot 10^{-8}$ [NM^{-2}]	$P_I \cdot 10^{-8}$ [NM^{-2}]	$2\alpha T$	N
0	283	5,190	3,633	0,700	1,105
	293	4,791	3,449	0,720	1,090
	303	4,431	3,271	0,740	1,070
	313	4,082	3,143	0,770	1,060
0,06	283	5,200	3,598	0,692	1,120
	293	4,849	3,442	0,710	1,107
	303	4,470	3,272	0,732	1,095
	313	4,100	3,099	0,756	1,080
0,25	283	5,250	3,465	0,660	1,127
	293	4,880	3,367	0,690	1,107
	303	4,500	3,204	0,712	1,100
	313	4,160	3,061	0,736	1,087
0,47	283	5,300	3,328	0,628	1,130
	293	4,930	3,229	0,655	1,115
	303	4,590	3,102	0,676	1,105
	313	4,240	2,968	0,700	1,093
0,66	283	5,340	3,257	0,610	1,137
	293	4,980	3,169	0,635	1,123
	303	4,675	3,048	0,652	1,114
	313	4,340	2,951	0,680	1,095
0,84	283	5,401	3,159	0,585	1,140
	293	5,071	3,118	0,615	1,129
	303	4,749	3,039	0,640	1,114
	313	4,430	2,923	0,660	1,098
1	283	5,530	3,124	0,565	1,171
	293	5,238	3,100	0,592	1,158
	303	4,900	3,013	0,615	1,145
	313	4,591	2,914	0,635	1,130

Table 1b

(carbon tetrachloride – butylic alcohol system)

$\chi_{ALCOHOL}$	T[K]	$P_{IW}\cdot10^{-8}$ [NM^{-2}]	$P_{I}\cdot10^{-8}$ [NM^{-2}]	$2\alpha T$	N
0	283	5,190	3,633	0,700	1,105
	293	4,791	3,449	0,720	1,090
	303	4,431	3,279	0,740	1,070
	313	4,082	3,143	0,770	1,060
0,05	283	5,210	3,594	0,690	1,108
	293	4,840	3,436	0,710	1,095
	303	4,480	3,270	0,730	1,081
	313	4,140	3,125	0,755	1,068
0,21	283	5,280	3,484	0,660	1,110
	293	4,970	3,404	0,685	1,100
	303	4,540	3,223	0,710	1,088
	313	4,220	3,089	0,732	1,072
0,41	283	5,410	3,381	0,725	1,120
	293	5,100	3,325	0,652	1,102
	303	4,640	3,132	0,675	1,092
	313	4,310	3,017	0,700	1,080
0,61	283	5,450	3,270	0,600	1,135
	293	5,090	3,191	0,627	1,120
	303	4,780	3,107	0,650	1,110
	313	4,450	3,003	0,675	1,100
0,81	283	5,540	3,185	0,575	1,147
	293	5,210	3,152	0,605	1,133
	303	4,920	3,084	0,627	1,125
	313	4,581	2,986	0,652	1,20
1	283	5,650	3,135	0,555	1,168
	293	5,340	3,123	0,585	1,150
	303	5,061	3,071	0,607	1,137
	313	4,700	2,946	0,627	1,122

In order to measure the ultrasound propagation velocity, the method of optical diffraction by an ultrasonic beam of 4 MHz frequency was used. Measurements were made for the determination of thermal expansion coefficients by means of a dilatometer, of the density by means of a picnometer and of molar capacity at constant pressure by means of an electrocalorimeter.

Table 1a, 1b and 1c contains the values we get for the real internal pressure, the van der Waals' pressure, calculated by relations (4) and (8) as well as that for the coefficients $2\alpha T$ and n.

Table 1c

(carbon tetrachloride – amilic alcohol system)

$\chi_{ALCOHOL}$	T[K]	$P_{IW}\cdot 10^{-8}$ [NM^{-2}]	$P_{I}\cdot 10^{-8}$ [NM^{-2}]	$2\alpha T$	N
0	283	5,190	3,633	0,700	1,105
	293	4,791	3,449	0,720	1,090
	303	4,431	3,279	0,740	1,070
	313	4,082	3,143	0,770	1,060
0,05	283	5,300	3,551	0,670	1,128
	293	4,980	3,436	0,690	1,112
	303	4,560	3,237	0,710	1,102
	313	4,200	3,107	0,740	1,090
0,18	283	5,370	3,436	0,640	1,131
	293	5,045	3,355	0,665	1,120
	303	4,650	3,208	0,690	1,105
	313	4,345	3,055	0,710	1,096
0,37	283	5,540	3,268	0,590	1,134
	293	5,200	3,208	0,617	1,128
	303	4,810	3,078	0,640	1,112
	313	4,480	2,948	0,658	1,102
0,57	283	5,680	3,152	0,555	1,138
	293	5,380	3,077	0,572	1,130
	303	4,971	2,967	0,597	1,116
	313	4,660	2,889	0,620	1,105
0,78	283	5,900	3,038	0,515	1,145
	293	5,580	3,013	0,540	1,140
	303	5,150	2,889	0,561	1,125
	313	4,820	2,815	0,584	1,112
1	283	6,180	3,028	0,490	1,185
	293	5,880	2,998	0,510	1,175
	303	5,400	2,862	0,530	1,160
	313	5,100	2,800	0,550	1,150

The survey of the results presented in this table reveals the decrease of the real internal pressure and of the van der Waals' ones with increasing temperature in all the studied systems.

The deviations of p_{iW} values from that of p_i which were evaluated by a more rigorous method are caused by the use of van der Waals' simplified model. This last is restrictive in character, in which molecular interactions are limited to those of dispersion and is based on a simplified model of molecules as concerning their shape and the number of interactions.

The values of the correction coefficients of the van der Waals' internal pressure, $2\alpha T$ and n, are smaller than one for the first of them and greater than one for the last one.

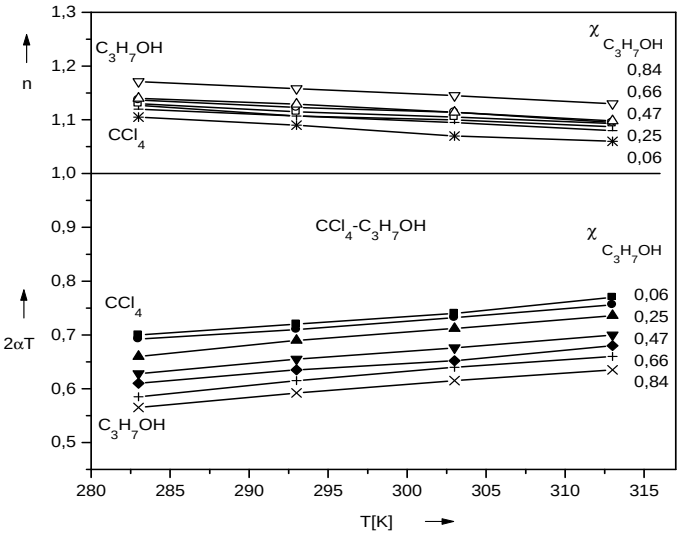

Fig. 1

The values of $2\alpha T$ smaller than one are in good agreement with $p_i < p_{iW}$; the decreasing contribution of $2\alpha T$ to the van der Waals' internal pressure with increasing temperature reflects the overlapping role of the rejection forces within the correction. The temperature increase concerns particularly the mentioned interactions, interactions which have not been included in the van der Waals' model.

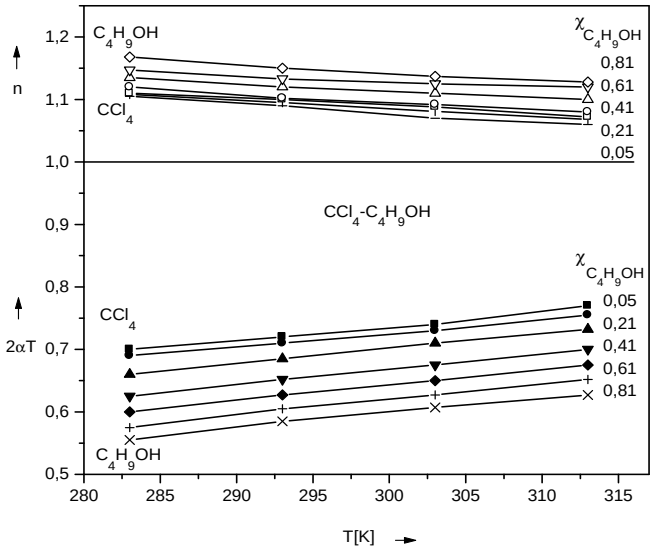

Fig. 2

In fig. 1, 2 and 3 the behaviour of the correction coefficients $2\alpha T$ and n as function of temperature is presented in the case of the three studied systems. The two coefficients vary linearly with temperature in opposite directions towards the same limiting value: $2\alpha T \rightarrow 1$, $n \rightarrow 1$. These dependencies show the evolution tendency of the liquid towards the van der Waals' model, as the temperature increases the reaching of the limit $2\alpha T = n = 1$ being impossible for the liquid phase.

At constant temperature, it can be observed the increase of correction coefficient n respectively the decrease of the correction coefficient $2\alpha T$ with increasing alcohol concentration for all studied systems, the changes being more pronounced as the molar mass of the alcohol increases.

In table 2 a comparative presentation of the two constants "a", from the van der Waals' formula of the internal pressure, respectively "a_c", the rectified one, are given as calculated by relations (6) and (14) for the studied systems. It has to be noticed the temperature independence of the constant "a_c".

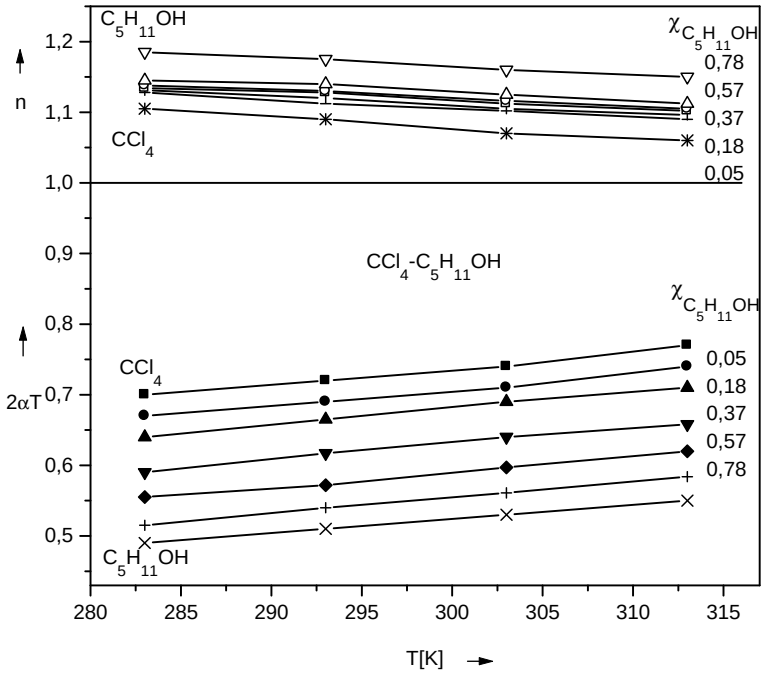

Fig. 3

Table 2

CARBON TETRACHLORIDE – PROPILIC ALCOHOL SYSTEM								
	T [K]	$\chi_{C_3H_7OH}$						
		0	0,06	0,25	0,47	0,66	0,84	1
$a \cdot 10^{-6}$	283	4,78	4,62	4,22	3,82	3,50	3,18	2,94
$[Nm^4kmol^{-2}]$	293	4,51	4,49	3,97	3,74	3,35	3,06	2,86
	303	4,25	4,22	3,81	3,55	3,23	2,92	2,80
	313	3,99	4,09	3,62	3,36	3,09	2,84	2,68
$a_c \cdot 10^{-6}$	283	3,25	3,01	2,70	2,45	2,18	1,97	1,67
$[Nm^4kmol^{-2}]$	293	3,25	3,00	2,70	2,46	2,17	1,98	1,68
	303	3,23	3,00	2,69	2,46	2,17	1,98	1,68
	313	3,22	3,01	2,69	2,45	2,17	1,97	1,69

carbon tetrachloride – butylic alcohol system								
	T [K]	$\chi_{C_4H_9OH}$						
		0	0,05	0,21	0,41	0,61	0,81	1
$a \cdot 10^{-6}$	283	4,78	4,60	4,51	4,58	4,75	4,60	4,62
$[Nm^4kmol^{-2}]$	293	4,51	4,43	4,41	4,40	4,53	4,41	4,44
	303	4,25	4,22	4,22	4,21	4,32	4,23	4,27
	313	3,99	3,98	3,97	4,03	4,21	4,07	4,15
$a_c \cdot 10^{-6}$	283	3,25	3,15	3,07	3,03	2,85	2,73	2,56
$[Nm^4kmol^{-2}]$	293	3,25	3,16	3,08	3,04	2,85	2,73	2,55
	303	3,23	3,16	3,08	3,04	2,86	2,74	2,56
	313	3,22	3,15	3,07	3,03	2,86	2,74	2,55
carbon tetrachloride – amilic alcohol system								
	T [K]	$\chi_{C_5H_{11}OH}$						
		0	0,05	0,18	0,37	0,57	0,78	1
$a \cdot 10^{-6}$	283	4,78	4,83	5,13	5,44	5,86	6,27	7,07
$[Nm^4kmol^{-2}]$	293	4,51	4,73	4,90	5,29	5,66	6,06	6,89
	303	4,25	4,47	4,63	5,00	5,40	5,79	6,52
	313	3,99	4,18	4,44	4,75	5,14	5,56	6,30
$a_c \cdot 10^{-6}$	283	3,25	3,04	3,17	3,31	3,51	3,64	3,58
$[Nm^4kmol^{-2}]$	293	3,25	3,04	3,18	3,30	3,51	3,64	3,58
	303	3,23	3,04	3,17	3,30	3,51	3,64	3,58
	313	3,22	3,03	3,17	3,29	3,50	3,65	3,59

REFERENCES

1) Jha D. K., Jha B. I., Acustica (Stuttgart), 75 (1992), p. 279
2) Lenart I., Ciupe A., Ausländer D., Academia Român¾, Comisia de Acustic¾, Caietul 24 (Bucure¿ti), (1994), p. 147-150
3) Ausländer D., Lenart I., Ciupe A., Acustica (Stuttgart), 81 (1995), p. 75 - 78
4) Hildebrand J. H., Scott R. L., Regular Solutions, Prentince Hall England Cliffs, (1962)
5) Mishra R. L., Some Acoustical and Thermodynamic Parameters, Doctor of Philosophy Thesis, Alahabad University, India, (1977)
6) Srinivasa Rao P., Sudha M. C. S., Naraiana Swamy G., Acustica (Stuttgart), 75 (1991), p. 86 - 89

STUDIA UNIVERSITATIS BABEŞ-BOLYAI, PHYSICA, XLXVIII, 2, 2003

THERMAL BEHAVIOUR OF SOME PYRAZINAMIDE COMPLEXES WITH TRANSITION METALS

V. SIMON, T. JURCA*

Faculty of Physics, Babes-Bolyai University, 3400 Cluj-Napoca, Romania
* Faculty of Medicine and Pharmacy, University of Oradea, 3700 Oradea, Romania

ABSTRACT. Pyrazinamide (PZA) is among the first-line drugs for the treatment of tuberculosis, which seems to reappear as a frequent disease. In this study is investigated the *thermal behaviour of* new transition metal complexes of PZA and *is searched* for a correlation between structure and thermal transformations, described as multi-step processes consisting in crystalline phase transition, decomposition, melting and thermo-oxidation.

Introduction

An increased incidence of tuberculosis in both developing and industrialized countries, a widespread emergence of multidrug-resistant strains and a deadly synergy with respect to the human immunodeficiency virus (HIV) have been observed in the last years [1, 2].

Pyrazinamide (pyrazine carboxamide, PZA) is a nicotinamide analogue, that has been used for almost 50 years as a first-line drug to treat tuberculosis [3]. PZA is bactericidal to semidormant mycobacteria and reduces the total treatment time [4, 5]. The parent molecule PZA and some of its complexes are widely used, due to their antimycrobial properties [6].

The present study is concerned in a series of transition metal complexes of pyrazinamide. The aim of this work is to study the thermal behaviour of these new complexes containing copper, cadmium and nickel.

Experimental

The parent pyrazinamide ($C_5H_5N_3O$) used for sample preparation is a Trans Medical Pharma reagent. The synthesis of the investigated complexes of pyrazinamide with transition metals was earlier reported [7]. The sample are transition metal tetrasulfocyanomercuryat complexes of pyrazinamide, $[Me(PZA)_nX_m]$, where Me = Cu, Cd or Ni and X = $[Hg(SCN)_4]^{2-}$, n = m =1 for Ni sample and n = 2, m=1 for Cu and Cd samples.

The copper chlorine complex of pyrazinamide $[Cu(PZA)_2Cl_2]$ was also investigated. All samples are powders. The structure of the samples was analysed by X-ray powder diffraction at room temperature (XRD) with a Bruker spectrometer.

Thermal analysis measurements were carried out using a MOM equipment. Thermogravimetric (TG), differential thermogravimetric (DTG) and differential thermal analysis (DTA) curves were recorded in the temperature range 20-1000^{0}C, with a rate of 10^{o}C/min.

Results and discussion

The thermogravimetric and differential thermal analysis curves inform on physical changes occurring in samples by heating. The thermal behaviour of the studied samples can be described as a multi-step process consisting in crystalline phase transition, decomposition, melting and thermo- oxidation.

Table 1.

Mass loss, melting / glass transition temperature of the investigated samples.

Sample	Mass Loss (%)	Decomposition Temperature (^{O}c)	Melting Temperature (^{O}c)	Glass Transition Temperature (^{O}c)
PZA	100	175	310	
$[Cu(PZA)_2Cl_2]$	87,4		290	
$[Cu(PZA)_n[Hg(SCN)_4]_m]$	81,7	180	260	
$[Cd(PZA)_n[Hg(SCN)_4]_m]$	84,8	240	245	
$[Ni(PZA)_n[Hg(SCN)_4]_m]$	89,1	250		290

After heating during the thermal analysis the mass loss was 100% for PZA, 87,4% for $[Cu(PZA)_2Cl_2]$, 81,7% for $[Cu(PZA)_n[Hg(SCN)_4]_m]$, 84,8% for $[Cd(PZA)_n[Hg(SCN)_4]_m]$ and 89,1% for $[Ni(PZA)_n[Hg(SCN)_4]_m]$ (Table 1). The thermogravimetric curve points out that the evaporation of pyrazidamine sample starts during the melting process. The mass losses reported for organolanthanide compounds containing the pyrazinamide ligand $LnCl_2Cp(PzA)_2$ (where Ln = Nd, Sm, Eu and Tb, Cp = cyclopeptadienyl and PzA = pyrazinamide) are ranging from 60.89 to 63.31% [8].

The DTA trace of PZA sample (Fig. 1) evidences two endothermic events with peak starting at 170 and 250^{o}C, having the minimum at 210 and 310^{o}C respectively. The first one is an endothermic crystalline phase transition peak [9]. The second endothermic peak is assigned to the sample melting and evaporation. The corresponding temperature is in good agreement with the data reported by other authors [10]. For $[Cu(PZA)_2Cl_2]$, $[Cu(PZA)_n[Hg(SCN)4]_m]$ and $[Cd(PZA)_n[Hg(SCN)_4]_m]$ samples only an endothermic event is observed (Fig. 2 - 4) and it was assigned to the sample melting. The minimum of the corresponding peaks, considered as melting temperature, and the mass losses by evaporation depend on the metallic cation and on its source (Table 1). For all samples, excepting $[Cu(PZA)_2Cl_2]$, before the endothermic peak an exothermic event is recorded accompanied by mass loss that could correspond to a sample decomposition.

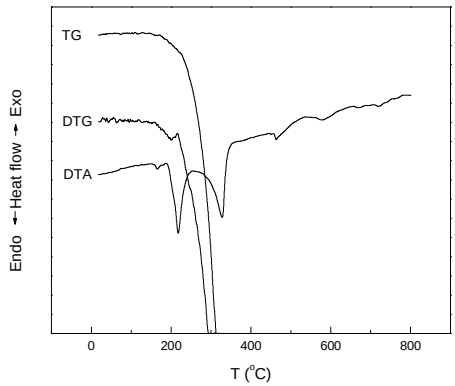

Fig. 1. Thermal analysis curves of PZA sample.

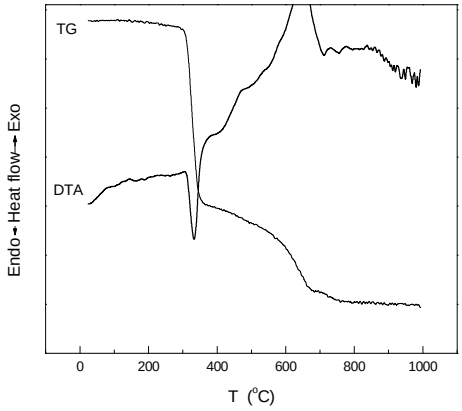

Fig. 2. Thermal analysis curves of $[Cu(PZA)_2Cl_2]$ sample.

Two exothermic events, partially superposed, with maxima between 440 and 570°C are recorded for all investigated organometallic samples. In the same temperature range the termogravimetric curves indicate a consistent mass loss. According to other authors [11], the two successive exothermic processes accompanied by mass losses could also consist in the thermo-oxidation of the sample in this temperature range.

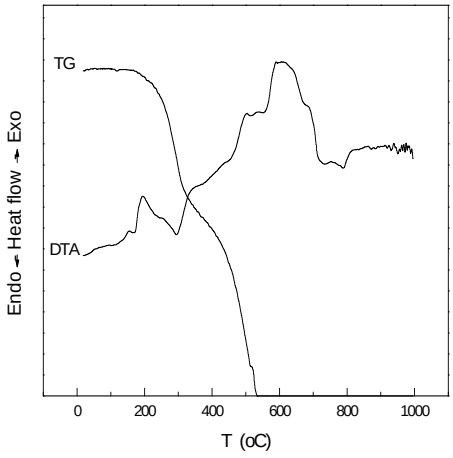

Fig. 3. Thermal analysis curves of $[Cu(PZA)_n[Hg(SCN)_4]_m]$sample.

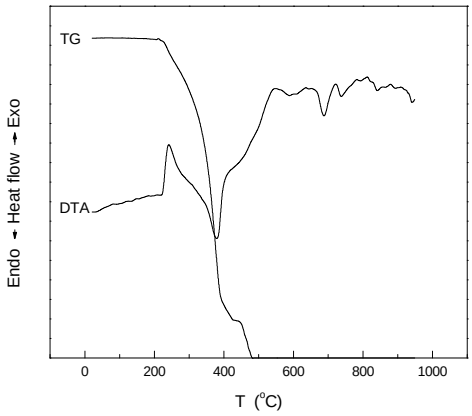

Fig .4. Thermal analysis curves of $[Cd(PZA)_n[Hg(SCN)_4]_m]$ sample.

For $[Ni(PZA)_n[Hg(SCN)_4]_m]$ sample no endothermic event occurs in the DTA trace (Fig. 5), but a glass transition process, with glass transition temperature at 290°C, is evidenced. The vitreous state of $[Ni(PZA)_n[Hg(SCN)_4]_m]$ sample was proved without doubt by X ray diffraction analyse (Fig. 6). The two exothermic events, partially superposed, could be supposed by the tendency of the remaining components to a higher order degree in two crystalline phases, but due to the consistent mass loss in the same temperature range indicated by TG curve they are assigned to the thermo-oxidation of the sample.

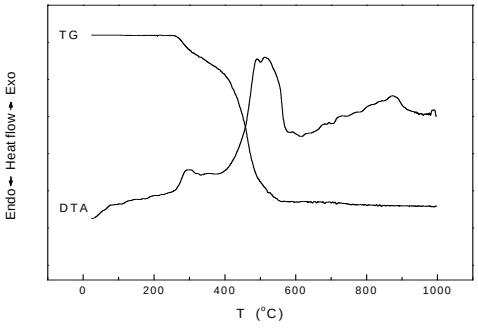

Fig. 5. Thermal analysis curves of $[Ni(PZA)_n[Hg(SCN)_4]_m]$ sample.

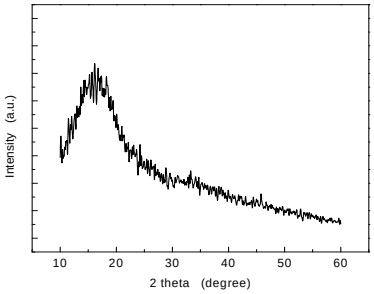

Fig. 6. X-ray diffraction pattern for $[Ni(PZA)_n[Hg(SCN)_4]_m]$ sample.

Conclusions

The mass loss after thermal analysis was 100% for PZA, 87,4% for $[Cu(PZA)_2Cl_2]$, 81,7% for $[Cu(PZA)_n[Hg(SCN)_4]_m]$, 84,8% for $[Cod(PZA)_n[Hg(SCN)_4]_m]$ and 89,1% for $[Ni(PZA)_n[Hg(SCN)_4]_m]$. The endothermic peak assigned to the sample melting and evaporation as well as the mass losses by evaporation depend on transition metal entering in pyrazinamide complex and on its source.

The thermal events evidenced in the DTA trace of $[Ni(PZA)_n[Hg(SCN)_4]_m]$ sample points out its vitreous state, in contrast with the crystalline state of the other transition metal pyrazinamide complexes. The thermal transformations of PZA-complexes with Cu and Cd can be described as a multi-step process consisting in crystalline phase transition, decomposition, melting and thermo-oxidation.

REFERENCES

1. M.C. Raviglione, C. Dye, S. Smidt, A. Kochi, *Lancet,* 35, 624 (1997)
2. S. Houston, A. Fanning, *Drugs*, 48, 689 (1996)
3. D. E. Snider, K.G. Castro, *New. Engl. J. Med*., 338, 1689 (1998)
4. L. Heifets, R. Lindholm-Levy, *Am. Rev. Respir. Dis*., 145, 1223 (1992)
5. D. A. Mitchison, *Natur. Med.,* 2, 6 (1996)
6. V.Opletalova, J.Hartl, A.Patel, K.Palat Jr., V.Buchta, *Il Farmaco*, 57, 135 (2002)
7. T. Jurca, *Analele Universitatii Oradea, Stiinte farmaceutice,* 1 (2002)
8. R.D.Miotti, A. de Sousa Maia, W. de Oliveira, *Quim. Nova*, 235, 5, 762 (2002)
9. G. Patrinoiu, L. Patron, O. Carp, N. Stanica, *J. Thermal Analysis and Calorimetry,* 72, 2, 489 (2003)
10. M. Dolezal, M. Miletin, Kunes, K. Kralova, *Molecules*, 7, 363 (2002)
11. P. Budrugeac, V.Trandafir, M.G.Albu, J. *Thermal Analysis and Calorimetry*, 72, 2, 581 (2003).

STUDIA UNIVERSITATIS BABEŞ-BOLYAI, PHYSICA, XLVIII, 2, 2003

THE ESTIMATION OF THE ABSORBED DOSES AND THE EVALUATION OF THE EXPOSURE IN THE NUCLEAR MEDICINE DIAGNOSIS PROCEDURES

ŞT. TAMÁS[1], O. COZAR[2], S. COTUL[1], M. DRAGOTEANU[1], CECILIA PÎGLEŞAN[1], NOÉMI TAMÁS[1]

[1] Nuclear Medicine Department / 3rd Medical Clinic, Clinical Hospital for Adult Patients, str. Croitorilor 19-21, Cluj-Napoca, Romania
[2] Department of Physics, Babeş – Bolyai University, str. Kogălniceanu 1, Cluj-Napoca

ABSTRACT. The paper presents MIRD method used in the nuclear medicine (NM) in order to estimate the absorbed dose in the human body as a consequence of administering different radiopharmaceuticals and to evaluate the effective dose (E) and the collective dose (***S***) received by the patients after using regular medicine procedures in the Nuclear Medicine Laboratory of the Clinical Hospital for Adult Patients Cluj in year 2000.

Keywords: internal exposure, MIRD, effective dose, collective dose

1. INTRODUCTION

The biological action of the nuclear radiations is due to the interaction between the radiations and the organism. This interaction, the ionization may induce chemical changes in some cells, changes which produce the partial or the total distruction of the cell and disfunctions of the organism.

The protection against injurious effects of the nuclear radiations includes a well-known aquaintance with the physical and biological factors that interfere in these phenomena, their quantification and the relations established between them.

The measurement of the absorbed dose in radioprotection is not enough because the biological effect in a tissue depends of the absorbed dose, the nature of the incident radiation and the radiosensibility of the tissue.

As a global evaluation of the interaction between radiation and environment, the radioprotection defines some terms which cannot be directly measured and which are indirectly deduced. These terms are: equivalent dose (H), effective dose (E), and (effective) collective dose (***S***) [1-4].

2. THE INTERNAL EXPOSURE

Some radioisotopes (labelled combinations with radioisotopes) participate to the human metabolism. The radioactiv nuclid or the combination that carries the radioisotope (radiopharamaceutical) – as a function of the biochemical properties – is accumulated in the organ, then the blood circuit transport it from a tissue to another, it is fixed in a certain tissue or it is eliminated in the air during the expiration process, or leaves the organism in the urine or in the excrements, in a longer or in a shorter period of time.

In order to describe the radiopharmaceutical accumulation and elimination from the organism, different mathematical models were elaborated, but the most used is the compartment model [5-7].

The evaluation of the absorbed doses in the human body after introducing a radiopharmaceutical in it needs physical, mathematical, chemical and biological information.

3. THE SNYDER ANTROPOMORPH PHANTOM

The most complex problem in the evaluation of the absorbed dose consists to determin the photon absorbtion in the organ. The values for this absorbtion may be evaluated with Monte-Carlo method, with the specific absorbtion fraction for a punctual source in an isotropic medium or with the reciprocity principle [8,9].

In order to solve all the aspects related with designing and evaluating the individual and the population protection against injurious effects of the nuclear radiations, ICRP (International Committee on Radiological Protection) set up a sub-committee which presented their results in 1975 in a paper [10], briefly entitled " The Reference Man". According to this paper, "the reference man" is 170 cm height, 70 kg weight and it is an hermaphrodite. Their data related to the organ measure, the distance between them, their spacial position, the parameter variation with the age, metabolic data are also synthetized in the same paper.

Based on these data related to "the reference man", Snyder and contributors made the antropomorph phantom (Fig. 1. a) [11], which was improved then by Cloutier and contributors (Fig.1.b) [6]. The phantom was built in order to follow the penetrating absorbed dose in a human geometry. The structure of the phantom idealizes and simplifies the human shape (e.g. there is only the shape of the head without the nose or the ears), but it allows the simulation on the computer.

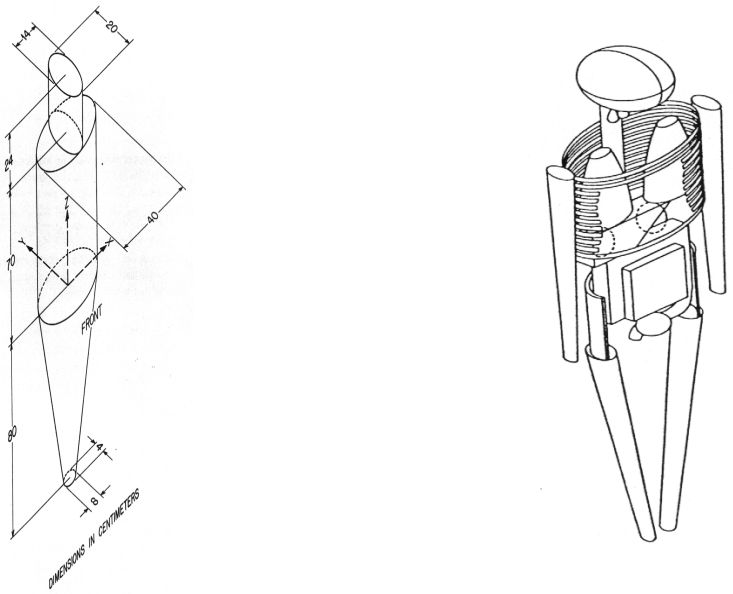

a b.

Fig. 1. Snyder phantom (MIRD-phantom) [6,11]
a) the whole body phantom
b) the internal organs phantom introduced in the whole body phantom

The same principle was also used for 22 internal organs, which present some subregions from the inside of the phantom.

It can be noticed that from the point of view of the internal parts there are three regions with specific densities: the skeleton (which includes the bones and the marrow) with $\rho=1.5g/cm^3$; the lungs region with $\rho=0.3g/cm^3$ and the other organs from the phantom with $\rho=1g/cm^3$ (water equivalent).

The heterogeneous phantom built this way is prepared for making Monte-Carlo estimations. With these estimations the authors followed "the faith" of 6.10^4 photons in each organ source and after this the computer listed the mean values of the absorbed energies (the absorbed fractions) in each spacial region defined (for each source-target pair). We underline that the results obtained with this method refers only to "the reference man". In reality, there is a large variety of individuals, beginning with the children of different ages for whom these results are not relevant/real. From this reason there are many techiques to transform the size of the absorbtion fraction – φ obtained in basis of "the reference man" data and extend the application aria of this method [4,12,13].

4. ESTIMATION OF THE ABSORBED DOSE – THE BASIC MIRD EQUATION

The estimation of the absorbed dose in the nuclear medicine procedures with MIRD (Medical Internal Radiation Dose Committee of the American Society of Nuclear Medicine) schema was introduced by Loevinger and Berman [8]. After them other authors extended the application aria of MIRD formalism, presenting different examples of estimation[14,15].

The basic MIRD equation is generaly written as:

$$\overline{\mathbf{D}}_{(T\leftarrow S)} = \widetilde{\mathbf{A}}_S . \mathbf{S}_{(T\leftarrow S)} \qquad (1)$$

The bar on D indicates a mean value and the tilda on A_S indicates the time integral. In consequence, $\overline{\mathbf{D}}_{(T\leftarrow S)}$ represents the medium absorbed dose (gray or rad) of the target organ T from a uniform distributed radionuclid in the source organ S. $\widetilde{\mathbf{A}}_S$ represents the cumulated activity in the source organ (becquerel-second or microcurie-hour) and $\mathbf{S}_{(T\leftarrow S)}$ represents the mean absorbed dose of the target organ from the source organ (gray/bequerel-second or rad/microcurie-hour), the last having a unitary cumulated activity. **S** is called "the **S** factor".

We underline that the biological and the metabolic data are included in the cumulated activity $\underline{A_S}$; the physical and the anatomical data are included in the second term of the equation, **S**.

THE CUMULATED ACTIVITY– $\widetilde{A}$

The cumulated activity of a source organ represents the number of nuclear changes in that source in a given period of time [5].

The variation of the cumulated activity in time in a mono-compartment system is described by a simple equation:

$$\widetilde{A}_S = \int_t A_S(t)dt \qquad (2)$$

The general equation which describes the activity in a source is:

$$A_S(t) = A_S(0)\sum_j \alpha_{sj} e^{-\lambda_{eff.j}t} \qquad (3)$$

where α is the fractional distribution function and **j** is the biological compartment.

For a given source organ:

$$\sum_j \alpha_{sj} = 1$$

α_{sj} = the fractional distribution function for a biological compartment j in the source organ

λ_{effj} = effective removal evacuation constant for a biological compartment **j** in the source organ

$\lambda_{effj}=\lambda_p+\lambda_{bj}$

λ_p = the decay constant

λ_{bj} = the biological removal constant

Solving the integral between 0 and ∞ the cumulated activity will be:

$$\widetilde{A}_S = 1{,}443 \cdot A_0 T_{eff} \qquad (4)$$

In order to simplify the estimation it is also used another notion: the residence time (τ) of a radioisotop in the source organ [5,14].

As a definition, the residence time is:

$$\tau_S = \frac{\widetilde{A}_S}{A_0} \qquad (5)$$

and the equation becomes:

$$\widetilde{A}_S = A_0 . \tau_S \qquad (6)$$

If $\mathbf{A_0}=1$ then

$$\widetilde{A}_S = \tau_S \qquad (7)$$

where:

τ_S = the residence time of the radioisotop in the source organ

$\mathbf{A_0}$ = the administrated activity

$\widetilde{A}_S$ = the cumulated activity in the source organ

THE ABSORBED FRACTION – φ

All the problems related to the doses estimation can be deduced from the following situation: let's consider an organ named source – S, which has the activity A, homogeneously distributed in the considered organ; the source organ irradiates another organ named target – T, which absorbes as ionization energy a part of the source energy as a consequence of the disintegration of the radioactiv nuclids. The ratio between the absorbed energy by the target organ – T and the emitted energy by the source – S represents the absorbed fractio [16,17], **φ**:

$$\varphi_{T-S} = \frac{\text{the energy absorbed by the target organ (T)}}{\text{the energy emitted by the source organ (S)}} \qquad (8)$$

The absorbed fraction depends of the radiation type according the following rules:

S ≠ T **φ** = 0 for a non-penetrating radiation

S = T **φ** = 1 for a non-penetrating radiation

S = T **φ** < 1 for a penetrating radiation

$$\mathbf{0 \le \varphi_i (T \leftarrow S) \le 1}$$

For γ radiations the absorbed fraction depends of the radiations energy, the shape and the size of the organs and of the geometrical configuration of the target and source organs. φ values are given in tables as a function of the gamma radiation energy [11,18].

THE SPECIFIC ABSORBED FRACTION – Φ

The specific absorbed fraction is the absorbed fraction of the target - source pair divided to the target mass [17]:

$$\Phi_{(T\leftarrow S)} = \frac{\varphi_{(T\leftarrow S)}}{\mathbf{m}_T} \qquad (9)$$

The shape of the target is not relevant here, the only condition is the mass to be part of the estimation model. The values of the specific absorbed fraction are presented in paper [10].

THE ABSORBED DOSE FROM THE ACCUMULATED ACTIVITY UNIT – S, (THE S FACTOR)

The **S** factor [17,19] is defined as:

S($T\leftarrow S$) [Gy/Bq.s or rad/μCi.h] or

$$\mathbf{S}(T \leftarrow S) = \sum_{\mathbf{i}} \Delta_{\mathbf{i}} \frac{\varphi_{\mathbf{i}}(T \leftarrow S)}{\mathbf{m}_T} \qquad (10)$$

i represents a certain type of radiation

$\Delta_{\mathbf{i}}$ = the equilibrium dose constant

$\varphi_{\mathbf{i}}(T\leftarrow S)$ = the absorbed energy fraction of a certain i radiation

$\mathbf{m_T}$ = the mass of the target organ[kg or g]

The equation of the **S** factor can be written as:

$$\mathbf{S}(T \leftarrow S) = \sum_{\mathbf{n}} \Delta_{\mathbf{n}} \frac{\varphi_{\mathbf{n}}(T \leftarrow S)}{\mathbf{m}_T} + \sum_{\mathbf{p}} \Delta_{\mathbf{p}} \frac{\varphi_{\mathbf{p}}(T \leftarrow S)}{\mathbf{m}_T} \qquad (11)$$

n and **p** in the equation correspond to the non-penetrating and penetrating radiation, respectively.

The values of the **S** factor for MIRD antropomorph phantom are given in tables for the radionuclids frequently used in nuclear medicine [19].

THE MEAN ENERGY PER NUCLEAR TRANSITION - Δ [20]

$$\Delta_{\mathbf{i}} = \mathbf{n}_{\mathbf{i}} \overline{\mathbf{E}}_{\mathbf{i}} \qquad (12)$$

$\Delta_{\mathbf{i}}$ = the dose constant at the equilibrium for an **i** type transition [kg.Gy/Bq.s or g.rad/μCi.h]

$\mathbf{n_i}$ = the mean number of particles or photons per nuclear transition

$\overline{\mathbf{E}}$ = the mean energy emitted by the source [J, MeV]

$\Delta_{\mathbf{i}}$ values can be estimated from the disintegration scheme.

The total energy emitted in a disintegration represents the sum of all **i** types of radiations emitted:

$$\Delta = \sum_{i} \Delta_i = \sum_{i} n_i \overline{E}_i \tag{13}$$

Dillman put in tables the Δ_i values for a big number of radionuclids [20-22].

The general equation MIRD which describes the absorbed dose by a target organ from a source organ has the following shape, as it was already shown:

$$\overline{D}_{(T \leftarrow S)} = \widetilde{A}_S . S(T \leftarrow S),$$

but in the most of the cases the target organ receives radiations which come from many sources. In these situations the equation becomes:

$$\overline{D}_T = \sum_{S} \overline{D}_{(T \leftarrow S)} \tag{14}$$

where the sum takes into consideration the contribution of each source S to the general irradiation of the target organ T.

At the end of this general presentation of the MIRD formalism, we have to underline that the results were obtained and put into tables in basis of "the reference man" model – the antropomorph phantom.

In reality, these data depends on the mass, the hight (volume), the sex, the age and the health of the patient. From this reason and making different researches on animals, building new phantoms of different dimensions (child phantom) with phantom organs having equivalent tissue composition, MIRD methodology extended its area of application [23].

In a given situation with well-known biological and anatomical conditions (the reference man), the mean absorbed dose in the target organ using relations (6) and (7) i

$$\overline{D}_T = S_{T \leftarrow S} \cdot \tau_S \tag{15}$$

If τ_S and $S_{T \leftarrow S}$ are known then the absorbed dose of an organ will be equivalent with the sum of the doses received from the other organs (including auto-absorbtion):

$$\overline{\mathbf{D}}_T = \sum_{\mathbf{S}} \tau_S \cdot \mathbf{S}_{T \leftarrow S}$$

For example: the liver is the target organ. In this case:

$$D_{Liver} = \tau_{Liver} \cdot \mathbf{S}_{Liver \leftrightarrow Liver} + \tau_{Spleen} \cdot \mathbf{S}_{Liver \leftarrow Spleen} + \tau_{Lungs} \cdot \mathbf{S}_{Liver \leftarrow Lungs} + \tau_{Stomach} \cdot \mathbf{S}_{Liver \leftarrow Stomach}$$

In most of the cases the **S** factor is written in tables and **τ** can be experimental determinated or can be taken from literature.

The estimation of the absorbed dose in organs can be done using succesive operations, taking into consideration physical and kinetic-radiopharmaceutical data as a function of the phenomenon nature. If a phenomenon in equilibrium is studied (like the fixation of the radiocolloids in RES cells) then the estimations are done with the mono-compartment model [5]. For dinamic complex phenomena (like secvential renal scintigraphy with ^{99m}Tc-DTPA) the description of the phenomena can be done using multi-compartment models [5,24].

In a similar way the absorbed doses in each organ can be estimated as a consequence of administering different radio-pharmaceuticals [25-28].

In practice it is enough to estimate the absorbed doses in the source organ, in the critical organ, in gonads and in the whole body if in the blood stays a significant percentage of radioisotops.

The nature of a biological effect produced by the absorbed doses varies with the nature of the incident radiation and with the radiosensibility of the tissue (organ), reason for which the equivalent dose (H) and the effective dose (E) [1-3] were defined.

The global effect (on the population) of the exposure on radiations because of a medical procedure or because of a source is a function of the number of exposed persons and the dose that they receive; this is the (effective) collective dose - ***S*** equivalent with the sum of the medium effective dose product received by different exposed groups and the number of individuals in each group, having as measurement unit sievert **.** person (Sv.person):

$$\boldsymbol{S} = \sum \mathbf{E_i}\, \mathbf{N_i} \qquad (17)$$

i = the group having $\mathbf{N_i}$ individuals uniform exposed to the effective dose $\mathbf{E_i}$.

Except the notions already mentioned, the international radioprotection standards work with other notions, too, like the limit dose, which is the value of the effective or equivalent dose reported to an individual or to an organ and which cannot be surpassed.

It is important to underline that the limit doses cannot be used in medical exposures. The international standards [3,29,30] recommend some specific doses for diagnosis and in the case of the radiotherapy with radioisotops the rules of irradiation are established in basis of other criteria that are not the objective of this paper.

5. RESULTS AND DISCUSSIONS

Tables 1 and 2 present the results of the absorbed dose in different organs using two models of estimation: the first one using a static planar liver-spleen scintigraphy after administering ^{99m}Tc-fitat (mono-compartment model) and the second one using a dynamic renal scintigraphy after administering ^{99m}Tc-DTPA (multicompartment model) [5,24].

Making the product between the absorbed dose of the organ and the weight factor of that tissue (organ) and making the sum between them, the effective dose (E) to which the patient was exposed during the investigation period was obtained.

Table 3 is a synthesis of the "in vivo" nuclear medicine procedures and the number of patients investigated in the Nuclear Medicine Laboratory of the Clinical Hospital for Adult Patients Cluj in year 2000 [31].

In order to process the data the patients were gathered after age, sex and procreation period: 16-40 years old and after 40 years old.

It is important to underline the big number of patients (40.73%, 1305 from 3204) who were investigated with ^{131}I-NaI for various tyroid affections, fact that has as consequence the raising of the collective dose on the population. It is also important to be notice that the "in vivo" NM procedures for children under 16 years old are better to be avoid for decreasing the exposure to radiation of this category.

Table 4 presents the effective doses E (mSv/MBq) and the effective dosees/procedure (mSv) absorbed by the patients in NM procedures with usual quantity of radiopharmaceuticals, doses evaluated in comparison with literature [10,14,17,19-22,30]. It was observed that the absorbed effective doses in "in vivo" NM procedures are bigger than the limit of 1 mSv/year, accepting the risk –

benefit principle. It was also observed that the examinations made with radiopharmaceuticals labelled with ^{99m}Tc are with at least one order less (1.8÷4.8 mSv) than the effective doses absorbed in a iodine-uptake or scintigraphy with ^{131}INa (16÷24 mSv).

Table 5 represents the contribution of each "in vivo" NM procedure in our laboratory to the internal exposure of our patients and the global contribution of the laboratory to the radiological exposure of the population. It is important to mention that the great majority of the collective exposures 92.7%, (44.712 Sv.person) comes from tyroid investigations with ^{131}I (tables 3 and 4) and it is a great necessity to change this procedure with other methods less injurious.

Table 1.

Radiation absorbed doses in various organs estimated after using hepato-splenic scintigraphy with ^{99m}Tc-phytat

ORGAN	ABSORBED DOSE	
	rad/mCi	μGy/MBq
Liver	0,322	87,00
Spleen	0,295	80,00
Marrow	0,032	8,70
Ovaries	0,006	1,60
Testes	0,001	0,32
Total body	0,027	7,30

Table 2

Radiation absorbed doses in various organs estimated after using sequential dinamic renal scintigraphy with ^{99m}Tc-DTPA

ORGAN	ABSORBED DOSE	
	rad/mCi	μGy/MBq
Kidneys	0,021	5,70
Ovaries	0,020	5,50
Testes	0,014	3,80
Urinary Bladder Wall	0,290	77,00
Total body	0,016	4,30

Table 3

Diagnostic nuclear medicine procedures and in vivo investigated patients performed at the Neclear Medicine Laboratory of the Clinical Hospital for Adult Patients Cluj in 2000 [31]

MEDICAL PROCEDURE	RADIO-PHARMACEUTICS		AGE AND SEX GROUP				NUMBER OF PATIENTS
	Type	Injected amount per procedure [MBq]	16 – 40 years		> 40 years		
			M	F	M	F	
Cerebral diffusion scintigraphy (planar and tomographic)	^{99m}Tc-DTPA	600	3	5	6	5	19
Lung perfusion scintigraphy	^{99m}Tc-MAA	150	3	3	8	5	19
Planar hepato-splenic scintigraphy	^{99m}Tc-Fitat	100	53	31	175	130	389
Angioscintigraphy and hepatic tomo-scintigraphy (SPECT)	^{99m}Tc-Fitat	400	6	14	45	54	119
Planar bone scintigraphy and whole body scintigraphy	^{99m}Tc-MDP	600	15	17	64	62	158
Sequential renal scintigraphy	^{99m}Tc-DTPA	150	22	19	49	51	141
Sequential hepatobiliary scintigraphy	^{99m}Tc-HIDA	80	1	1	2	8	12
Sequential oesophagus scintigraphy	^{99m}Tc-Fitat ^{99m}Tc-DTPA	80	1	-	4	4	9
Sequential parotid scintigraphy	^{99m}Tc-pertechnetat	80	1	4	1	2	8
Sequential rectoportoscintigraphy	^{99m}Tc-pertechnetat	400	5	2	17	8	32
Thyroid scintigraphy	^{131}I-Na	1,5	21	432	29	511	993
Thyroid radioiodine uptake	^{131}I-Na	1,0	56	461	67	721	1.305
Total nr. of patients			187	989	467	1.561	3.204

Table 4

Effective doses (E) and doses per in vivo MN procedure (E/procedure) in various diagnostic medical explorations performed at the Neclear Medicine Laboratory of the Clinical Hospital for Adult Patients Cluj in 2000 [31]

MEDICAL PROCEDURE	RADIOPHARMACEUTICS		E [MSV/MBQ]	E /PROCEDURE [MSV]
	TYPE	INJECTED QUANTITY PER PROCEDURE [MBQ]		
Cerebral diffusion scintigraphy (planar and tomographic)	99mTc-DTPA	600	0,0063	3,78
Lung perfusion scintigraphy	99mTc-MAA	150	0,0120	1,80
Planar hepato-splenic scintigraphy	99mTc-Fitat	100	0,0280	2,80
Angioscintigraphy and hepatic tomoscintigraphy (SPECT)	99mTc-Fitat	400	0, 0280	11,20
Planar bone scintigraphy and whole body scintigraphy	99mTc-MDP	600	0,0080	4,80
Sequential renal scintigraphy	99mTc-DTPA	150	0,0063	0,95
Sequential hepatobiliary scintigraphy	99mTc-HIDA	80	0,0240	1,92
Sequential oesophagus scintigraphy	99mTc-Fitat 99mTc-DTPA	80	0,0280 0,0063	2,24 0,50
Sequential parotid scintigraphy	99mTc-pertechnetat	80	0,0053	0,42
Sequential rectoportoscintigraphy	99mTc-pertechnetat	400	0,0053	2,12
Thyroid scintigraphy	131I-Na	1,5	16,0	24,00
Thyroid radioiodine uptake	131I-Na	1,0	16,0	16,00

Table 5

Effective dose (E) and (effective) collective dose *(S)* in different nuclear medicine procedures (imaging and nonimaging procedures) performed at the Neclear Medicine Laboratory of the Clinical Hospital for Adult Patients Cluj in 2000 [31]

MEDICAL PROCEDURE	RADIO-PHARMACEUTICS	E [MSV]	NUMBER OF PATIENTS	S [MSV.PERS]
Cerebral diffusion scinti-graphy (planar and tomo-graphic)	^{99m}Tc-DTPA	3,78	19	71,82
Lung perfusion scinti-graphy	^{99m}Tc-MAA	1,80	19	34,20
Planar hepato-splenic scintigraphy	^{99m}Tc-Fitat	2,80	389	1.089,20
Angioscintigraphy and hepatic tomoscintigraphy (SPECT)	^{99m}Tc-Fitat	11,20	119	1.332,80
Planar bone scintigraphy and whole body scinti-graphy	^{99m}Tc-MDP	4,80	158	758,40
Sequential renal scinti-graphy	^{99m}Tc-DTPA	0,95	141	133,95
Sequential hepato-biliary scintigraphy	^{99m}Tc-HIDA	1,92	12	23,04
Sequential oesophagus scintigraphy	^{99m}Tc-Fitat ^{99m}Tc-DTPA	1,35	9	12,15
Sequential parotid scintigraphy	^{99m}Tc-pertechnetat	0,42	8	3,36
Sequential rectoportoscintigraphy	^{99m}Tc-pertechnetat	2,12	32	67,84
Thyroid scintigraphy	^{131}I-Na	24,0	993	23.832
Thyroid radioiodine uptake	^{131}I-Na	16,0	1.305	20.880
Summa			3.204	48.238,76 ~48.240 mSv.pers
Collective dose – S = 48.24 Sv . pers				

6. CONCLUSIONS

- The paper studied the contribution of the NM diagnosis procedures to the patients internal exposure. We mention that we did not consider the contribution of the therapeutic methods with radio-isotops and those radiological of external exposure.
- The results (especially the collective doses) allow a comparison between all the laboratories with the same profile in the country and abroad and also the comparison of NM Laboratory of the Clinical Hospital for Adult Patients Cluj contribution to the medical exposure of the population at national level.
- Making these studies every year, the efficiency of our laboratory can be controled during the years.
- Gathering all the results from each NM and radiology laboratory, the risk factor produced by the medical diagnosis exposure of the Romanian people can be estimated.
- Taking into consideration the ^{131}I contribution to patients exposure during the investigation of different tyroid affections and the major contribution of this radioisotop to the collective dose compared with radiopharmaaceuticals marked with ^{99m}Tc (tables 4 and 5), knowing the experience of the developed countries, it is important that the tyroid morphologic exploration (scintigraphy) with ^{131}I to be changed with 99m-Tc and the functional examination, with "in vitro" testes (radioimmunological – RIA – methods).

REFERENCES

1. M., Oncescu, Conceptele radioprotecței, Ed. Horia Hulubei, Bucureşti – Măgurele, 1996
2. Norme fundamentale de securitate radiologică, Monitorul Oficial al României, Partea I, Anul XII. Nr. 404bis/2000
3. International Basic Safety Standard for Protection against Ionising Radiation and for the Safety of Radiation Sources. Safety Series No. 115, IAEA, Vienna, 1996
4. P.B., Zanzonico, J. Nucl. Med., 41, 297, (2000)

5. G.F., Fueger, W., Schreiner, Dosimetrie Offener Radionuklide, Ed. Informatica Gesellschaft m.b.H, Wien, 1985, pp. 78-95, 193-207
6. R.J., Cloutier, E.E., Watson, J.L., Coffey, Radiopharmaceutical dose calculation, in J. Harbert da Rocha AFG. Eds. Textbook of Nuclear Medicine. Vol.1 Philadelphia: Lea & Febiger, 1984. pp. 267-282
7. M., Berman, Kinetic Models for Absorbed Dose Calculations, NM/MIRD Pamphlet N°12, Society of N.M., New York, 1976
8. R., Loevinger, M., Berman, MIRD Pamphlet N°1, J. Nucl. Med. Suppl. N°1/1968
9. W.H., Ellett, Application of gamma-ray diffusion theory to radiation dosimetry, Ph. D. thesis, Univ. of London, 1968
10. ICRP Publication N°23, Report of the Task Group on Reference Man, Pergamon Press, New York, 1975
11. W.S., Snyder et al., MIRD Pamphlet N°5, J. Nucl. Med. Suppl. N°3/1969,
12. K.S., Kolbert, G., Sgouros, A.M., Scott et al., J. Nucl. Med., 38, 301 (1997)
13. J.A., Siegel, S.R., Thomas, J.B., Stubbs et al., MIRD Pamphlet N°16, J. Nucl. Med. Suppl. N°2/1999
14. R., Loevinger, T., Budinger, E., Watson, MIRD Primer for Absorbed Dose Calculation, The Society of Nuclear Medicine, New York, 1988
15. W.E., Bolch, L.G., Bouchet, J.S., Robertson et al., MIRD Pamphlet N°17, J. Nucl. Med. 40, 11S (1999)
16. G.L., Brownell, W.H., Ellett, A.R., Reddy, MIRD Pamphlet N°3, J. Nucl. Med. Suppl. N°1/1968
17. W.S., Snyder, M.R., Ford, G.G., Warner, MIRD Pamphlet N°5 (revised), Society of Nuclear Medicine, New York, 1978
18. W.H., Ellett, R.M., Humes, MIRD Pamphlet N°8, J. Nucl. Med. Suppl. N°5/1971
19. W.S., Snyder, M.R., Ford, G.G., Warner, S.B., Wattson, MIRD Pamphlet N°11, Society of Nuclear Medicine, New York, 1975
20. L.T., Dillman, MIRD Pamphlet N°4, J. Nucl. Med. Suppl. N°2/1969
21. L.T., Dillman, MIRD Pamphlet N°6, J. Nucl. Med. Suppl. N°4/ 1970
22. L.T., Dillman, F.C., Von der Lage, MIRD Pamphlet N°10, The Sosiety of Nuclear Medicine, New York, 1975
23. T., Smith, N., Petroussi-Henss, M., Zankl, Eur. J. Nucl. Med., 27, 1387 (2000)
24. M.G., Stabin, A., Taylor Jr., D., Eshima, W., Wooter, J. Nucl. Med. 33, 33 (1992)

25. L., Johansson, S., Mattson, B., Nosslin, Leide-Sveghorns, Eur. J. Nucl. Med., 19,933 (1992)

26. R.J., Cloutier, E.E., Watson, R.H., Rohrer, E.M., Smith, J. Nucl. Med. 14, 53 (1973)

27. S., Ertl, H., Deckart, A., Blottner, M., Tautz, Nucl. Med. Communications, 8, 643 (1978)

28. D.A., Weber, P., Todd Makler, E.E., Watson et al., J. Nucl. Med., 30, 1117, (1989)

29. Recommendation of the International Commission on Radiological Protection – Publication N°60 (ICRP-60/1990), Pergamon Press, Oxford & New York, 1991

30. M.G., Stabin, J.B., Stubbs, R.E., Toohey, Radiation Dose Estimates for Radiopharmaceutecals, Ed. Radiation Internal Dose Information Center, Oak Ridge Institute for Science and Education, 1996

31. Şt., Tamás, Determinarea fixării radiocoloizilor în organe şi iradierea în medii biologice neomogene – Teză de doctorat, Univ. "Babeş-Bolyai", Cluj, 2002

STUDIA UNIVERSITATIS BABEŞ-BOLYAI, PHYSICA, XLXVIIII, 2, 2003

SUBSTITUTION EFFECT ON STRUCTURE AND LEACHING PROPERTIES OF PHOSPHATE GLASSES

D. MUREŞAN, D. ENIU*, V. SIMON

Babes-Bolyai University, Faculty of Physics, 3400 Cluj-Napoca, Romania
[*]University of Medicine and Pharmacy, Faculty of Pharmacy, 3400 Cluj- Napoca, Romania

ABSTRACT. Two phosphate glass matrices were investigated in order to estimate the effects of substitutions both for glass former and for glass modifier on glass transition temperature and leaching properties of samples. In [$10K_2O \cdot 90P_2O_5$] matrix the phosphorus oxide was partially replaced by CaO up to 35 mol % while in the calcium-phosphate glass matrix [$40CaO \cdot 60P_2O_5$] the calcium oxide was progressively stubtituted by Al_2O_3 up to 15 mol %. The effects consist in the increase of glass transition temperature for the samples of the first system and the decrease of glass transition temperature in the second system. At the same time differences in the leaching behaviour of the two systems are observed.

Introduction

Over the past two decades a general experimental and theoretical framework has been developed for understanding the corrosion behaviour of glass in aqueous environments [1-4]. In recent years phosphate glasses have been extensively studied as suitable glasses for delivering of cations. Simple phosphate glasses do not have enough chemical durability for such applications. However, new systems of phosphate glasses, that slowly release active ingredients [5-7], are used to cure trace element deficiencies in animals and as agricultural fertilizers.

Experimental

The investigated samples belong to $xCaO(90-x)P_2O_5 \cdot 10K_2O$ ($0 \le x \le 35$) and $xAl_2O_3(40-x)CaO\ 60P_2O_5$ ($0 \le x \le 15$) systems. They were obtained from homogenized mixtures of $CaCO_3$, $(NH_4)_2HPO_4$, K_2CO_3 and Al_2O3 reagents of p.a. purity grade by melting at 1100^oC for 10 minutes in sintered corundum crucibles in an electric furnace and quickly undercooling at room temperature by pouring onto stainless steal plates.

The thermal analysis TG, DTG and DTA curves were recorded in the temperature range $20\text{-}1000^0C$ by using a MOM equipment, with a heating rate of 10^oC/min.

The corrosion behaviour was followed in static regime by immersion of samples in decationised water. The mass of samples was measured after different immersion times, by using an analytic balance sensitive to 0.1mg. The glass surface area to solution volume ratio was around 15 m^{-1} for all samples.

Results and discussion

The X ray difraction (XRD) patterns of investigated samples consist of a broad line centered around $2\theta = 29^o$, typical of vitreous systems, as shown in Fig. 1 for the $K_2O\text{-}CaO\text{-}P_2O_5$ system. The patterns do not evidence any narrow line of crystalline phases.

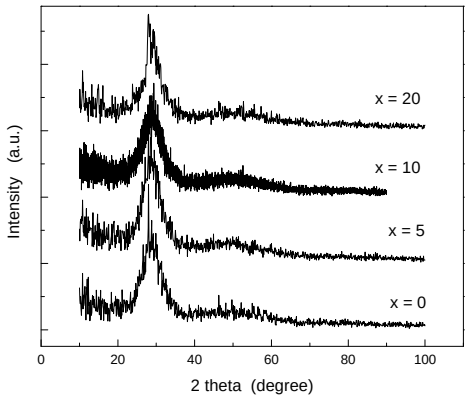

Fig. 1. XRD patterns of some $xCaO(90-x)P_2O_5 \cdot 10K_2O$ samples.

The glass transition temperature, T_g, corresponding to the quasi-endothermic peak from differential thermal analysis (DTA) curves are ploted in Figs 2 and 3. One remarks the different effects of substitutions carried out in the two glass systems. The addition of calcium to the potassium phosphate matrix, on the account of glass former, leads to the increase of glass transition temperature while the addition of aluminium to the calcium phosphate matrix, on the account of glass modifier, leads to the decrease of glass transition temperature. The results obtained for the first system are in agreement with the values reported for Na_2O-CaO-P_2O_5 glasses [8]. The termogravimetric data indicate mass loss for all CaO-K_2O-P_2O_5 samples due to loss of water. An endothermic peak occurring in DTA curves at 120^oC was also assigned to water release from the hygroscopic samples, as can be seen in Fig. 4.

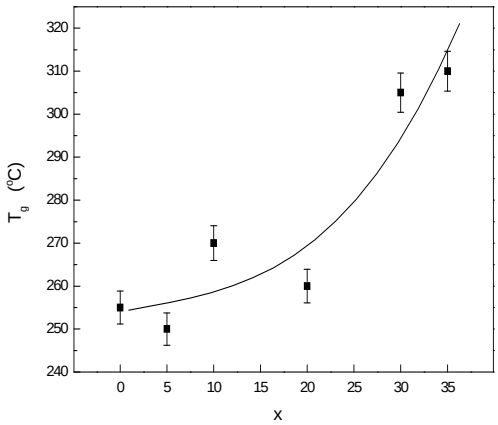

Fig. 2. Composition dependence of glass transition temperature for x$CaO\cdot(90-x)P_2O_5\cdot 10K_2O$ glass system. The line is only guide for eyes.

The results obtained in the leaching test carried out at room temperature in static regime indicate that the dissolution rate corresponds to the expected behaviour [11]. In order to explain the different release of cations from the glass network in the investigated dissolution media beside the composition of glasses and solvents is necessary to take into account the short range order characterizing the samples. The structural stability of cations in glass matrices is correlated with their local symmetry [4].

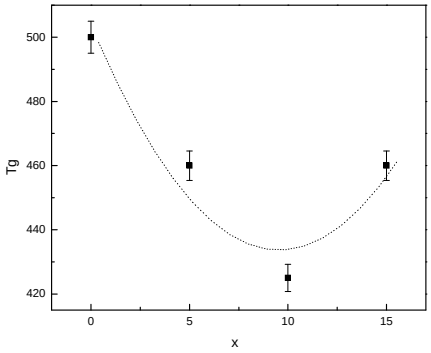

Fig. 3. Composition dependence of glass transition temperature for $xAl_2O_3(40\text{-}x)CaO{\cdot}60P_2O_5$ glass system. The line is only guide for eyes.

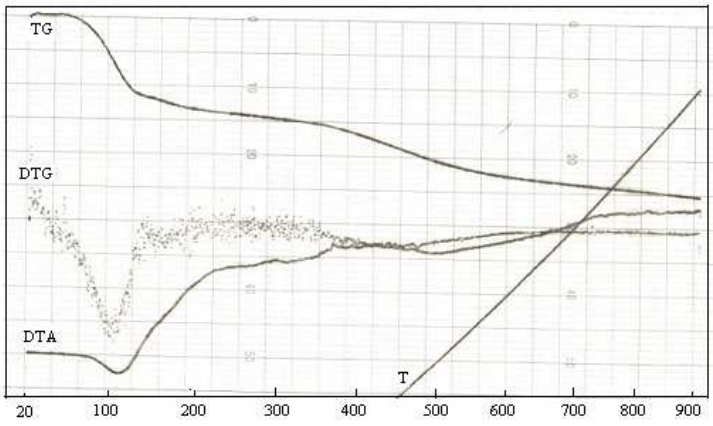

Fig. 4. Thermal analysis curves for $10CaO{\cdot}80P_2O_5{\cdot}10K_2O$ sample.

Pure vitreous P_2O_5 consists in a continuous random network (polymeric structure) of quasi-tetrahedral PO_4 units wherein phosphorous is four coordinated and only three of the oxygen atoms of each unit bridge to neighbouring units, while the forth is doubly bonded to the central phosphorous atom. The presence of the modifier like alkali and alkaline earth species decreases the number of bridging oxygens (P-O-P bridge) in PO_4 units, while its negative charge increases.

Two PO_4 tetrahedra sharing an oxygen, that can be represented as $(PO_3)^{2-}$ –O– $(PO_3)^{2-}$, form the $(P_2O_7)^{4-}$ pyrophosphate anions. Both in the melt and during the quenching process will occur an equilibrium between the pyrophosphate anions and their products as follows [12] $(PO_3)^{2-}$ –O– $(PO_3)^{2-} \leftrightarrow (PO_4)^{2-}$ + –O– $(PO_2)^{-}$.

The dissolution resistance has to be also related to the presence of K_2O and CaO in the investigated glass matrices, having in view that the alkali ions diminish the network consistency [13].

No mass loss was recorded for the samples belonging to Al_2O_3-CaO-P_2O_5 system up to 100 hours test time. For CaO-K_2O-P_2O_5 system the dependence of the relative mass loss on the increasing CaO content during leaching in decationised water is illustrated in Fig. 5. In the investigated time range one observes two leaching stages relative to the incipient dissolution. In the first stage the lowest release rate is obtained from the potassium-phosphate matrix (x = 0) and from the samples with low CaO content (x. ≤ 10). In the second stage the cations release is proportional to CaO content.

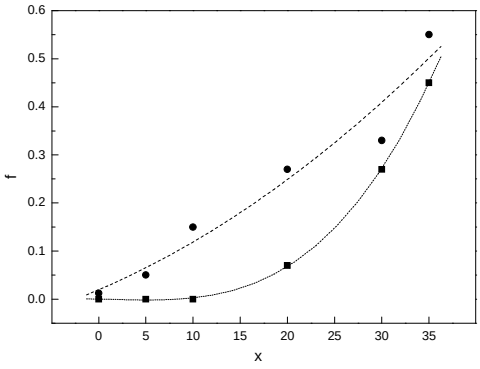

Fig. 5. Composition dependence of the relative mass loss of x$CaO\cdot(90\text{-}x)P_2O_5\cdot10K_2O$ glass samples after: 4 hours (▪) and 7 hours (●) in desalinised water. The lines are only guide for eyes.

The initial stages of the aqueous reactions always results in the leeching of alkali and alkaline earth species from the surface of the glass to create a P_2O_5-rich surface layer. It is generally believed that in the initial stages of the leaching reaction, the contact of liquid water or vapour water with the glass surface leads to an exchange of alkali and alkaline earth ions in the glass with hydrogenated ions in

the aqueous environment. (i.e., ion exchange or interdiffusion mechanism). Another mechanism proposed is based on the diffusion of molecular water into the glass and its chemisorption at the non-bridging oxygen (NBO) sites where alkali and alkaline earth species reside in the glass [14].

Two possible structures for the surface layer have been proposed [15]. In one case the layer has a network molecular structure that is a relic of the original glass molecular structure except that the alkali and alkaline earth ions have been replaced by a hydrogen ion plus one or more water molecules. This structure has been refereed to as “hydrogen" glass. In the other case, the hydrogen glass may transform over time by localized hydrolysis and condensation reactions into a silica-gel like layer. The exact composition structure and extent of the surface layer depend upon the details of the contacting environment as well as the structure and composition of the original glass.

In the investigated $xCaO\cdot(90\text{-}x)P_2O_5\cdot 10K_2O$ system, the network structure of potassium phosphate glass was systematically varied by the direct substitution of calcium oxide for phosphorous oxide with maintaining of constant K_2O concentration. This substitution causes the elimination of non-bridging oxygen (NBO) sites in the potassium phosphate matrix. The concentration of NBO sites influences the reaction rate with water from the leaching solutions as well as the diffusivity of water and released cations. The calcium itself influences the corrosion behaviour because it introduces new sites in the glass network.

Conclusions

The substitution effects on glass transition temperature are oposite in the two phosphate systems investigated. T_g increases by glass former substitution in $K_2O\text{-}P_2O_5$ matrix and decreases by glass modifier substitution in $CaO\text{-}\ P_2O_5$ matrix.The release rate of cations from $xCaO\cdot(90\text{-}x)P_2O_5\cdot 10K_2O$ glasses indicates that the corrosion behaviour of the samples depends on glass composition and local structure.The $xAl_2O_3(40\text{-}x)CaO\ 60P_2O_5$ ($0 \le x \le 15$) samples are very stable in water up to 100 hours, as evidenced by the leaching test carried out in static regime at room temperature.

5. REFERENCES

1. P. Bailif, J.C. Touray, Glass Science and Technology, 5, 161 (1999)
2. T.A. Guiton, C.G. Pantano,Coll. Surf. A, 74, 33 (1993)
3. P.J. Hamilton, C.G. Pantano, J. Non-Cryst. Solids, 222, 167 (1997)
4. P.J. Hamilton, PhD Thesis, The Pennsylvania State University, 1999
5. C.F. Drake, W.M. Allen, Biochem. Soc. Trans., 13, 516 (1985)
6. J. Burnie J, T. Gilchrist, S.R.I. Duff, et al., Biomaterials, 2, 244 (1981)
7. P. Knott, Glastech Ber., 62, 29 (1989)
8. M. Uo, M. Mizuno, Y. Kuboki, A. Makishima, F. Watari, Biomaterials, 19, 2277 (1998)
9. R. El-Mallawany, Proc. Int. Congr. Glass, Vol. 2., Edinburgh, Scotland, 1-6 July 2001.
10. R.K. Brow, D.R.Tallant, J.J. Hudgens, et al., J.Non-Cryst. Solids, 177, 221 (1994)
11. V. Simon, D. Cacaina, D. Muresan, S. Simon, 12-th EPS Conference, Budapest, 2002, p. 437
12. A.M.Efimov, J. Non-Cryst. Solids, 209, 209 (1997)
13. H. Li, M. Tomozawa, J. Non-Cryst. Solids, 195, 188 (1996)
14. B.M.Smets, T.P.A.Lommen, Phys. Chem. Glasses, 23, 83 (1982)
15. R.H.Doremus, Glass Science, John Wiley and Sons Inc., 1994, p.215.

STUDIA UNIVERSITATIS BABEŞ-BOLYAI, PHYSICA, XLXVIIII, 2, 2003

RELEASE BEHAVIOUR AND LOCAL STRUCTURE OF Ag_2O-CaO-Bi_2O_3-B_2O_3 GLASSES

V. SIMON, R. STEFAN, E. INDREA

Babes-Bolyai University, Faculty of Physics, 3400 Cluj-Napoca, Romania
[*]University of Agricultural Sciences and Veterinary Medicine, 3400 Cluj-Napoca, Romania
[**]National Institute for Research and Development of Isotopic and Molecular Technologies, 3400 Cluj-Napoca, Romania

ABSTRACT. Quaternary Ag_2O-CaO-Bi_2O_3-B_2O_3 glasses are investigated with regard to release behaviour and local structure. The dissolution behaviour in water and physiological serum shows that the cations are released rapidly or gradually and points out a multi-step process generally characterised by higher rates in water than in physiological serum. The effect of silver addition to bismuth-borate glasses with low lime content on their structure is evidenced from X-ray scattering measurements. The addition of silver leads to a diminution of the atom packing in this system. The atoms from the third and forth coordination spheres occur in a less distorted configuration than in the precursor CaO-Bi_2O_3-B_2O_3 vitreous compound.

Introduction

Glass systems allowing controlled release of components are intensely investigated [1-3] in the last decades. Various inorganic antibacterial materials containing silver have been developed and some of them are in medical use. The silver ions got released show an excellent antibacterial property [4]. Silver is capable of killing over 650 different forms of bacteria and viruses [5, 6]. Bismuth trace element is used for eye/ear infection and sore throats. The antibacterial activity of bismuth is also known [7, 8]. Although boron is potentially toxic to all organisms, and, as boric acid and borax, has been used as a pesticide and food preservative, higher animals usually do not accumulate boron because of their ability to rapidly excrete it [9]. It appears that boron may influence the production of hormones, including the active D vitamin form, improve brain and psychological functions, and exert immune-boosting activity [10]. Calcium is essential for all forms of life. It occurs in cell walls and bones. It is important for blood clotting and it is implied in the

complicated mechanisms of long term memory and learning [11, 12]. The aim of this paper is to investigate the dissolution behaviour and the antibacterial effects of quaternary Ag_2O-CaO-Bi_2O_3-B_2O_3 system both for glass and vitroceramic samples in correlation with their structure.

Experimental

The investigated $xAg_2O \cdot (4.76\text{-}x)CaO \cdot 14.29Bi_2O_3 \cdot 80.95B_2O_3$ system ($0.95 \leq x \leq 3.81$ mol %) was obtained from homogenized mixtures of $AgNO_3$, $CaCO_3$, $Bi(NO_3)_3 \cdot 5H_2O$ and H_3BO_3 reagents of p.a. purity grade by melting at 1050^{o}C for 15 minutes in sintered corundum crucibles in an electric furnace and quickly undercooling at room temperature by pouring onto stainless steal plates. All as prepared samples were transparent and colorless or slight jellowish.

The corrosion behavior was followed in static regime by immersion of disk samples in different solvents simulating biological media (desalinized water, physiological serum and chlorine acid solution with pH = 1.5) by measuring the mass of samples maintained in the mentioned solutions incubated at 40^{o}C for different times up to 68 hours. The samples mass was determined by using an analytic balance sensitive to 0.1mg. The glass surface area to solution volume ratio was around 15 m^{-1} for all samples.

Results and discussion

Quantitatively, corrosion stability is usually expressed via the mass decrease as a result of a treatment in an aggressive medium in a given time interval, or by selective determination of the components that have passed into solution. The rate of dissolution (DR) can be expressed either as $\frac{\Delta m}{S \cdot M \cdot \Delta t}$ or $\frac{\Delta m}{S \cdot \Delta t}$, where Δm is the mass change during the dissolution time Δt, S is the sample surface and M is the molar mass of the sample. In this study was used the last equation.

The results of the corrosion test carried out in water and physiological serum are shown in Figures 1 and 2. The dissolution rate decreases in water from the average value 5 μg/cm^2·min to 0.5 μg/cm^2·min as the Ag_2O content in sample increases from 1.90 to 3.81 % mol, while in physiological serum the DR values are constant lower, under 1 μg/cm^2·min, excepting the sample with 3 mol % Ag_2O for which DR_{av} = 2.6 μg/cm^2·min. Mass losses could not be measured after immersion in HCl solution because all sampled softened in the first 15 hours.

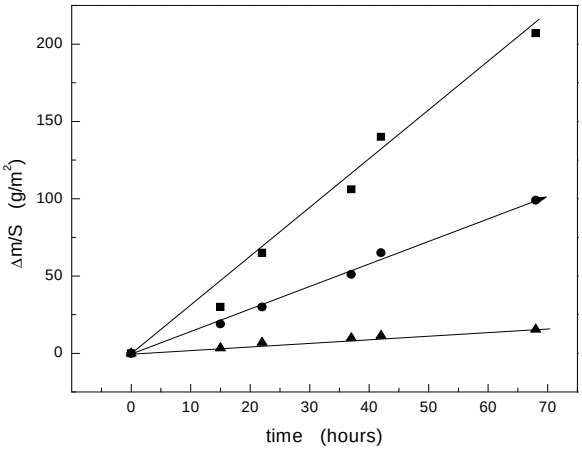

Fig. 1. Time dependence of the specific mass loss in water for $xAg_2O·(4.76-x)CaO·14.29Bi_2O_3·80.95B_2O_3$ glass samples with x = 1.90 (■), x = 2.86 (●) and x = 3.81 (▲). The lines are only guide for eyes.

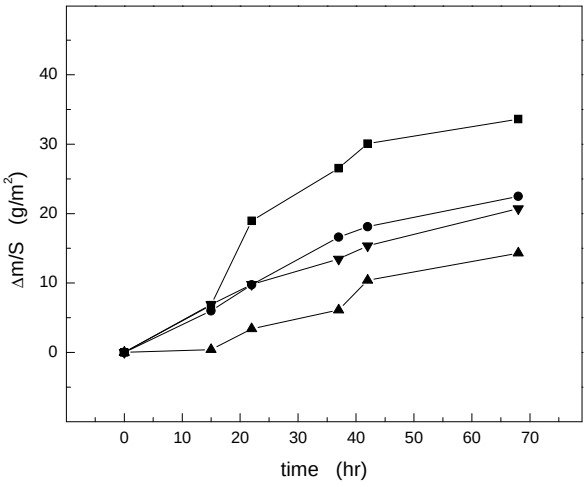

Fig. 2. Time dependence of the specific mass loss in physiological serum from $xAg_2O·(4.76-x)CaO·14.29Bi_2O_3·80.95B_2O_3$ glass samples with x = 0.95 (■), x = 1.90 (●), x = 2.86 (▲) and x = 3.81 (▼) . The lines are only guide for eyes.

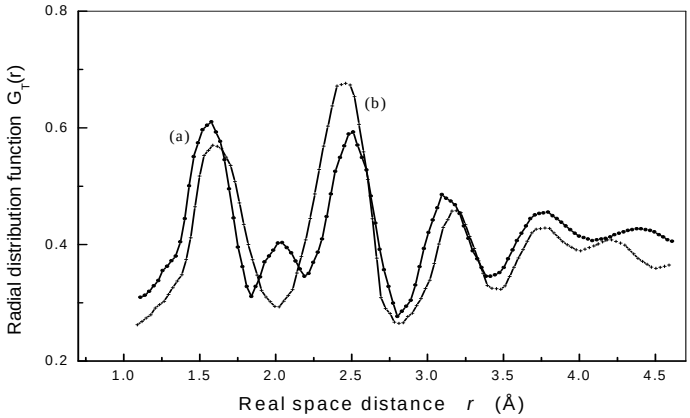

Fig. 3. Total atomic distribution function, $G_T(r) = 4\pi r^2 \cdot [\rho(r)]$, for samples with x=1.90 (a) and x=3.81 (b) of $xAg_2O \cdot (4.76\text{-}x)CaO \cdot 14.29Bi_2O_3 \cdot 80.95B_2O_3$ vitreous system.

In order to explain the different release of cations from the glass network in the investigated dissolution media beside the composition of glasses and solvents is necessary to take into account the short range order characterizing the samples. The structural stability of cations in glass matrices is correlated with their local symmetry [13]. The local order in glass and crystalline compounds of the same composition has both similarities and differences. The differences are assigned to the loss of long range order, to the deviation from a perfect crystalline structure. The atoms arrangement in the first coordination sphere is determined by the chemical composition and peculiarities of chemical bonds and generates the local order around them, that is very important to depict the vitreous systems. There are also glass systems wherein the local structure is extended at more than some coordination spheres imposing a middle or intermediate range order [14].

The structure of $xAg_2O \cdot (4.76\text{-}x)CaO \cdot 14.29Bi_2O_3 \cdot 80.95B_2O_3$ system was investigated by analysing the atomic radial distribution function obtained from X ray scattering data using a PEDX program [15]. The atomic pair correlation function for the silver containing bismuth-borate glasses with x = 1.90 and x = 3.81 are presented in Figure 3. The atom pairs correlation function shows maxima and their position, width and area are determined by the distribution of atom

pairs in the structural disordered sample. The real space distance corresponding to the maxima determined from the data obtained in this study may be compared with results reported for other similar systems [16-20] and allow to identify the atom pairs orderly disposed in the investigated system. They are summarised in Table 1. From the recorded peaks it was also found that B-O distances are 1.38 Å and O-O distances are 2.8 Å. Inspecting the data obtained for the samples with 1.90 and 3.81 mol % Ag_2O from the analysis of atom pairs correlation function one remarks the occurrence of Ca – B pair as a first coordination formation, well composed at a distance of 1.95 – 2.0 Å. The analyses indicated a rearrangement of these atom pairs as the calcium atoms content decreases in the vitreous system. The distances *r* between Ca – B, B – B and Bi – B pairs are ranging from 2.4 to 2.8 Å and become higher with the silver oxide content from glass samples, while the changes observed for the atoms from the third and forth coordination sphere are very slight. The silver addition to the calcium-bismuth-borate precursor glass preserves the vitreous structure, that evidences the high ability of the precursor glass to accept relatively high Ag_2O content without structural changes. One also notices a diminution of the atom packing in this system containing silver. This effect is evidenced by the larger radius values obtained for the first coordination spheres.

Table 1.

Atom pairs orderly disposed in the vitreous system, identified from the analysis of atom pairs correlation function.

COORDINATION SPHERE	ATOM PAIRS	X (MOL %)		DISTANCE (Å)
I	Ca – B Ca - B	1.90	3.81	1.954 2.014
II	Ag – B B – B			2.849 2.856
III	Bi - B Bi - B			3.536 3.575
IV	Ag - Ag			4.161

The further atoms from the third and forth coordination spheres occur in a less distorted configuration than in the precursor CaO-Bi_2O_3-B_2O_3 vitreous compound.

Conclusion

The release behaviour of $xAg_2O \cdot (4.76\text{-}x)CaO \cdot 14.29Bi_2O_3 \cdot 80.95B_2O_3$ vitreous system in water and physiological serum indicates a multi-step process generally characterised by higher rates in water than in physiological serum. The addition of Ag_2O to the lime-bismuth-borate matrix influences the dissolution rate of samples due to increase of distances between Ca – B, B – B and Bi – B pairs in the first coordination spheres and to diminution of the atom packing with the increasing silver content. X-ray scattering results indicate that the silver addition to the calcium-bismuth-borate precursor glass preserves the vitreous structure, evidencing the high ability of the precursor glass to accept relatively high Ag_2O content without structural changes. A diminution of the atom packing in the samples containing silver is also evidenced. The distances between Ca – B, B – B and Bi – B pairs are ranging from 2.4 to 2.8 Å and become higher with the silver oxide content.

REFERENCES

1. M. Otsuka, M. Sawada, Y. Matsuda, et al., Biomaterials, 18, 23, 1559 (1997)
2. F. Delahaye, L. Montagne, G. Palavit, J.C.Touray, P. Baillif, J. Non-Cryst. Solids, 242, (1998)
3. D. Arcos, C.V. Ragel, M. Vallet-Regi, Biomaterials, 22, 701 (2001)
4. M. Kawashita, Tsuneyama, F. Miyaji, et al., Biomaterials, 21, 4, 393 (2000)
5. Gerald H. Smith : Health & Happ., vol. 4, 2 (1998)
6. Manjubala and T.S. Sampath Kumar, Biomaterials 21, 19, 1995 (2000)
7. Gorbach, SL, NA Cornick, M Silva, Rev. Infect. Dis., 12, 21 (19900
8. N.A. Cornick, M. Silva, S..L Gorbach, . Rev. Infect. Dis., 12, 9 (1990)
9. W.D. Loomis WD, R.W. Durst , BioFactors, 3, 229 (1992)
10. J.G. Penland, Biol. Trace Elem. Res., 66, 299 (1998)
11. K.T. Blackwell, T.P. Vogl, D.L. Alkon, Computational Neuroscience, 137 (1998)
12. K.T. Blackwell, D.L. Alkon., J. Neurosci., 24, 17 (1998)
13. P.J. Hamilton, PhD Thesis, The Pennsylvania State University, 1999
14. R. E. Youngman, S. T. Haubrich, J. W. Zwanziger, et al., Science 269, 1416(1995)

15. V. Petkov, Y. Waseda, PEDX: a program for radial-distribution function analysis of energy-dispersive X-ray diffraction data from disordered materials
16. R.J. Angel, Min. Mag. 49, 37 (1985)
17. A.S. Rizkalla, D.W. Jones, D.B. Clarke, G.C. Hall, J. Biomed. Matter. Res., 32 119 (1996)
18. J. Swenson, L Börjeson, R.L. McGreevy, W.S. Howells, Phys. Rev. B55, 17, 11236 (1997)
19. R.L. Mozzi, B.E. Warren, J. Appl. Cryst., 3, 251 (1970)
20. I. Ardelean, E. Indrea, Rev. Rom. Phys., 23, 10, 165 (1978)